ERK-mediated Curvature Feedback Regulates Branching Morphogenesis in Lung Epithelial Tissue

*Tsuyoshi Hirashima[1,2,3] and Michiyuki Matsuda[2,4,5]

1. The Hakubi Center, Kyoto University, Kyoto, Japan
2. Laboratory of Bioimaging and Cell Signaling, Graduate School of Biostudies, Kyoto University, Kyoto, Japan
3. Japan Science and Technology Agency, PRESTO, Kawaguchi, Japan
4. Department of Pathology and Biology of Diseases, Graduate School of Medicine, Kyoto University, Kyoto, Japan
5. Institute for Integrated Cell-Material Sciences, Kyoto University, Kyoto, Japan

ORCID
TH: 0000-0001-7323-9627
MM: 0000-0002-5876-9969

*Corresponding author: Tsuyoshi Hirashima, Ph.D

The Hakubi Center/Graduate School of Biostudies, Kyoto University
Yoshida-Konoe-cho, Sakyo-ku, Kyoto 606-8501, Japan
Phone: +81-75-753-4422
hirashima.tsuyoshi2m@kyoto-u.ac.jp

Abstract

Intricate branching patterns emerge in internal organs because of the repetitive presence of simple deformations in epithelial tissues. During murine lung development, epithelial cells in distal tips of a single tube require fibroblast growth factor (FGF) signals generated by their surrounding mesenchyme to form repetitive tip bifurcations. However, it remains unknown how the cells employ FGF signaling to convert their behaviors to achieve the recursive branching processes. Here we show a self-sustained epithelial regulatory system during the murine lung branching morphogenesis, mediated by extracellular signal-regulated kinase (ERK), which acts as a downstream driver of FGF signaling. We found that tissue-scale curvature regulates ERK activity in the lung epithelium using two-photon live cell imaging and mechanical perturbations. ERK is activated specifically in epithelial tissues with a positive curvature, regardless of whether the change in curvature was attributable to morphogenesis or artificial perturbations. Moreover, we found that ERK activation accelerates actin polymerization specifically at the apical side of cells, and mechanically contributes to the extension of the apical membrane, leading to a decrease in epithelial tissue curvature. These results indicate the existence of a negative feedback loop between tissue curvature and ERK activity beyond scale. We confirmed that this regulation was sufficient to generate the recursive branching processes by a mathematical model. Taken together, we propose that ERK mediates the curvature feedback loop underlying the process of branching morphogenesis in developing lungs.

Keywords: Branching morphogenesis, ERK, FRET cell imaging, lung development, mathematical model, self-organization

Introduction

Characteristic patterns are generated in developing tubular organs through the repeated occurrence of tissue morphogenetic modes, such as elongation, bending, and bifurcation [1–4]. During murine lung development, the complex branched architecture is stereotypically created from a simple epithelial tube, by assembling morphogenetic modes as building motifs with a spatio-temporal order [2]. Previous genetic studies have revealed the essential molecules and signaling pathways underlying lung epithelial morphogenesis [5–7]. Moreover, previous studies have proposed how cellular behaviors and mechanical forces determine the tube shape [8–10]. Thus, the interplay between chemical signals and cell mechanics in constituent cells determines the organized periodic branched pattern, though it is not completely understood yet.

Several pharmacological and genetic studies have demonstrated that fibroblast growth factor (FGF) signaling is a key regulator of lung branching morphogenesis during murine development [11]. The treatment of an isolated epithelium in which the mesenchyme is removed with different FGF ligands has clarified the distinct roles of FGFs in lung epithelial morphology. For example, FGF1 and FGF10 induce bud formation, while FGF7 gives rise to a balloon-like shape, and any of these ligands could promote epithelial proliferation [12–14]. An investigation of the spatio-temporal expression pattern uncovered the fact that *Fgf10* is expressed locally in the mesenchyme surrounding the distal bud of the lung epithelium [14], and its main receptor, *Fgfr2b*, is homogeneously expressed in the lung epithelium [12]. These results led to hypothesize that the *Fgf10* prepattern initiates branching during lung development [14]; this was partially supported by results of previous studies on mice in which *Fgf10* or its main receptor *Fgfr2b* were knocked out and showed the complete absence of lungs [15–17]. However, it was demonstrated that the ubiquitous overexpression of *Fgf10* in its knocked out background could restore the branching process [18], indicating that the *Fgf10* expression is required but the precise prepattern is dispensable for the murine lung branching morphogenesis. Thus, we explored how FGF signals are converted to cellular behaviors underlying tissue morphogenesis.

A main FGF downstream signaling pathway, the extracellular signal-regulated kinase ERK/MAP kinase pathway, includes a three-tiered kinase cascade, i.e., RAF - MEK – ERK [11]. The genetic inactivation of either *Mek1/2* or *Erk1/2* specifically in the airway epithelium results in lung agenesis [19], implying that ERK and its activation were essential for lung development [20]. Previously, immunofluorescence staining results suggested that the phosphorylation of ERK was most likely to occur in the distal tips of the lung epithelium, and may thus be involved in the budding process during lung development [21–23]. FGFR2-mediated ERK activation reportedly upregulates the expression of *Anxa4*, whose products are able to bind with F-actin

bundles, and promote cell migration within epithelial tissues [22]. These reports revealed the role of ERK activity in cellular behavior during lung development. However, it is still unclear how the epithelial cells collectively behave to generate the periodic branching morphogenesis mediated via ERK signaling.

In this study, we show a physical basis for self-sustained branching morphogenesis by combining two-photon live cell imaging of a Förster resonance energy transfer (FRET)-based biosensor, mechanical perturbation, and mathematical modeling. We found that ERK activation occurs specifically in epithelial tissues with a positive curvature, and promotes cell extension through actin polymerization at the apical edges, resulting in a decreased tissue curvature. Thus, our study clarifies that the negative feedback loop between the tissue curvature and ERK activity underlies the process of repetitive branching morphogenesis in developing murine lung epithelial tissues.

Results

1. ERK activation occurs in distal tips of lung epithelial tissue

We first examined the impact of ERK activity on lung epithelial morphology during murine development. We cultured developing murine lungs dissected at embryonic day (E) 12.5 in the presence or absence of PD0325901, an inhibitor of the ERK activator MEK, under explant culture conditions. The growth of 1-day cultured lung epithelial tissues was remarkably impaired by the inhibition of ERK activity (Figure 1A, 1B), indicating the importance of ERK activation for epithelial morphogenesis during this stage.

Then, we visualized the spatial distribution of ERK activity in lung lobes dissected from murine embryos that ubiquitously expressed the FRET biosensor for the ERK activity [24–26] via whole tissue two-photon live imaging (Figure 1C, Movie 1). FRET images showed that the ERK activity in the epithelium was highly dependent on tissue curvature; the ERK activity was higher in the curved sheet protruding the mesenchyme (convex), while it was lower in the sheet bent towards the lumen (concave) (Figure 1C). Although endothelial cells exhibited relatively high levels of ERK activity, they were less involved in epithelial branching morphogenesis [27]; thus, we focused on ERK activity in epithelial tissues. The basal surface of epithelial tissue was extracted for quantification, and positions at nodes of generated meshes were embedded on the surface, enabling us to map chemical and geometrical quantities, such as ERK activity, epithelial tissue curvature, and tissue thickness (Figure 1D, S1A). As expected, there was a positive correlation between the ERK activity and tissue curvature ($\rho=0.51$, where ρ is the Spearman's rank correlation coefficient; Figure 1E, 1G, S1B), which indicates that ERK activation would occur mainly in convex regions. Moreover, there was a negative correlation between the ERK activity and tissue thickness ($\rho=-0.48$; Figure 1F, 1G). As observed in distal buds, the epithelial tissue was thinner in the tip region, where ERK was activated, than in the stalk region, where ERK was inactivated (Figure 1H). These results suggest the existence of interplay between the ERK activity and cell morphology in developing murine lungs.

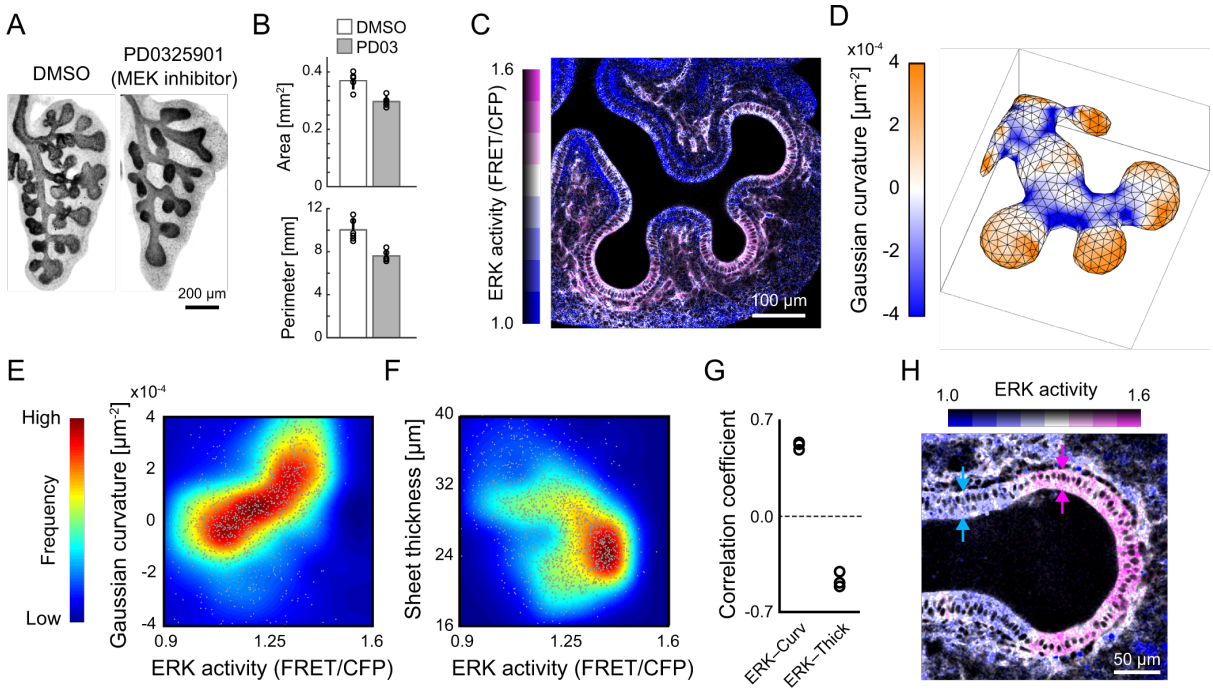

Figure 1 Relationship between ERK activity and tissue geometry in the lung epithelium
(A) Immunofluorescence images of anti-E-cadherin staining in an ex vivo culture of lungs for 1 day from E12.5, after treatment with dimethyl sulfoxide (DMSO) (left) and 1 µM PD0325901 (right). Scale bar, 200 µm. (B) Area and perimeter of epithelial tissues from the projected images. Data represent mean and standard deviation (SD) values. N=6, two-sample t-test, $p<0.001$.
(C) Representative ERK activity map in a developing lung at E12.5. Scale bar, 100 µm.
(D) Gaussian curvature map on the basal side of lung epithelial cells.
(E, F) Scatter plot of ERK activity versus Gaussian curvature (E) and that of ERK activity versus sheet thickness (F). Color indicates frequency. n=427, N=3.
(G) Correlation coefficient of (E) and (F). N=3, one-sample t-test, p=0.001 (E), and p=0.004 (F).
(H) ERK activity map in the distal region of a lung dissected at E12.5. Arrows facing each other indicate the sheet thickness at a tip (magenta) and distal stalk (blue). Scale bar, 50 µm.

142 **2. ERK activity follows the morphological change of isolated epithelial tissues**

143 To analyze how ERK activity is regulated in the lung epithelium, we isolated epithelial tissues
144 from mesenchymal tissues, and embedded them in Matrigel with culture media containing
145 FGFs for ex vivo culture (Figure 2A). This simplified experimental system allows us to explore
146 responses to external chemical and mechanical stimuli in epithelial cells under regulated
147 conditions. As reported previously [12,13], treatment with 500 ng mL^{-1} FGF1 for 1 day induces
148 branched epithelial buds, while that with 100 ng mL^{-1} FGF7 gives rise to a cyst-like structure
149 with an enlarged lumen (Figure 2B). PD0325901 treatment with FGF1 results in the collapse
150 of the lumen and absence of large deformations; this was also observed with the absence of
151 growth factors with 1-day-old culture (Figure 2B). We then examined the spatial distribution
152 of ERK activity in epithelial tissues, 1 hour after chemical treatment. FGF1 activates ERK
153 exclusively at the distal buds, in a manner similar to that observed with the mesenchyme
154 (Figure 1C), through ligand endocytosis from the basal side of cells (Figure S2, Movie 2),
155 despite the homogeneous expression of four FGF receptors, i.e., FGFR1, FGFR2, FGFR3, and
156 FGFR4 in the distal epithelial tissues [12,18,28,29]. In contrast, FGF7 activates the ERK almost
157 homogeneously in the epithelial tissues (Figure 2C). As expected, ERK activity was
158 homogeneously low in epithelial cells treated with PD0325901 or cultured without any growth
159 factors (Figure 2C). These results suggest that localized ERK activation at the distal tips is key
160 to the process of branching morphogenesis.

161 To examine the spatio-temporal dynamics of ERK activity during the branching of
162 isolated epithelial tissues, we performed two-photon live imaging under FGF1 supplemented
163 conditions. We found that the ERK activity increased during the protrusion of epithelial tips,
164 and decreased when the tip apex became flat during the tip bifurcation process (Figure 2D,
165 Movie 3). Notably, no mesenchymal cells were observed around the distal tip of the epithelium
166 (Figure 2D), suggesting that tip bifurcation could occur in a self-sustaining manner without
167 mesenchymal cells. The quantification of the ERK activity and tissue curvature at the tip apex
168 shows that the decrease in ERK activity follows that in curvature, with an average delay of 97
169 min (Figure 2E, 2F). This observation suggests that the ERK activity is controlled by the
170 curvature of the epithelial cells.

171 To clarify the morphological differences in cells between the convex and concave regions
172 of epithelial tissues, we measured the basal and apical areas of epithelial cells through whole-
173 tissue staining using E-cadherin. The basal cell area of isolated epithelial tissues in the convex
174 region is significantly larger than that in the concave region (Figure 2G, left), while the apical
175 cell area in the convex region is almost equivalent to that in the concave region (Figure 2G,

176 right). The epithelial basal edges act as an interface for cells to receive growth factor signals
177 from external environments that activate ERK (Figure S2). Therefore, we speculate that the
178 extension of basal membranes would trigger ERK activation in the convex regions of epithelial
179 tissues.
180

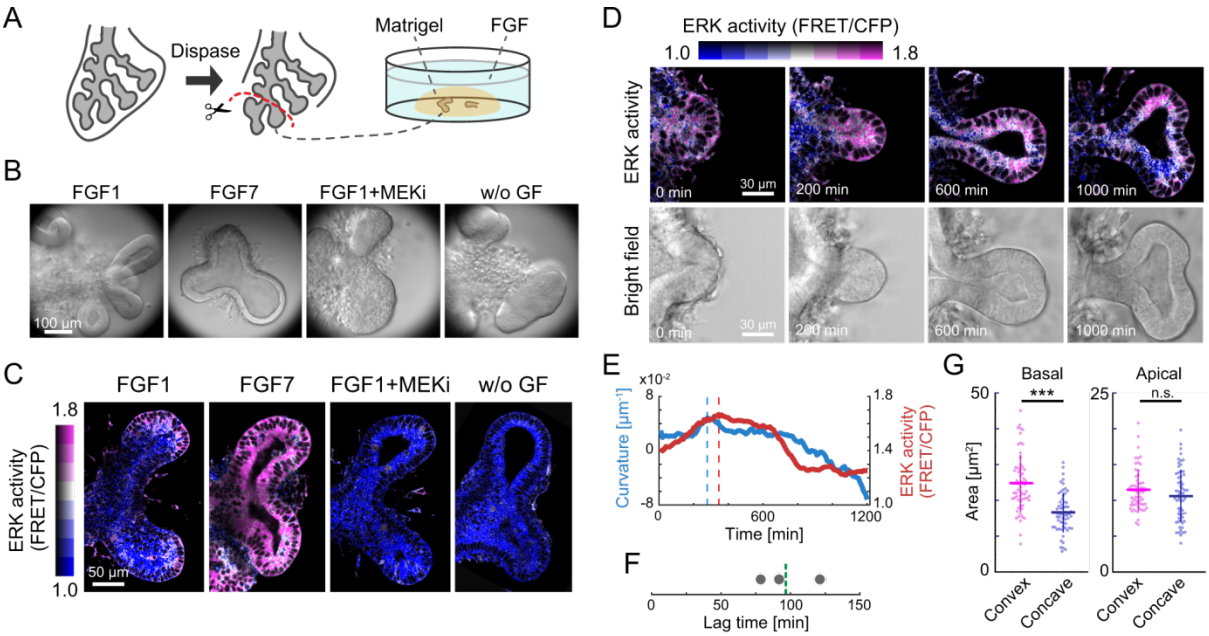

181
182

183 **Figure 2 ERK activity and tissue curvature in isolated epithelial cells**
184 (A) Schematics of the culture system for isolated lung epithelial tissues.
185 (B) Bright field images of isolated epithelial tissues subjected chemical treatments for 1 day
186 from E12.5. Concentrations: 500 ng mL^{-1} FGF1, 100 ng mL^{-1} FGF7, 1 µM PD0325901 (MEKi).
187 Scale bar, 100 µm.
188 (C) ERK activity of isolated epithelial tissues subjected to chemical treatments shown in (B)
189 for 1 hour from E12.5. Scale bar, 50 µm.
190 (D) Time-lapse images of ERK activity (upper) and bright field (lower) during terminal
191 bifurcation of lung epithelial tissues. Scale bar, 30 µm.
192 (E) Tissue curvature (blue) and ERK activity (red) at the tip apex over time (E). Vertical dotted
193 lines indicate the peak time for the tissue curvature and ERK activity, respectively.
194 (F) Lag time from the peak for tissue curvature to the peak for ERK activity. N=3.
195 (G) Basal area (left) and apical area (right) of individual cells in the convex and concave
196 regions of isolated epithelial tissues. Bold and error bars represent the mean and SD values,
197 respectively. n=60, N=3. Welch's t test, $p<0.001$ (left) and $p=0.18$ (right).
198

199 **3. The shape of epithelial tissues controls the ERK activity**

200 To test whether the shape of epithelial tissues controls the ERK activity, we performed a
201 physical perturbation assay using isolated epithelial tissues. We embedded isolated epithelial
202 tissues within the FGF1-containing Matrigel filled inside a polydimethylsiloxane (PDMS)
203 chamber, and uniaxially compressed it by 33% either parallelly or vertically to the distal-
204 proximal axis of the lung epithelium (Figure 3A). Time-lapse images obtained during this
205 process allow us to examine the ERK activity response to perturbations in different axes
206 (Figure 3B, 3C). For parallel compression, the curved epithelial tissues at the tip apex became
207 flattened (Figure 3D) and ERK activity decreased exclusively in the flat region (Figure 3E,
208 Movie 4). However, for vertical compression, the tip apex of the epithelium became sharp
209 (Figure 3D) and ERK activation followed the change in tissue curvature (Figure 3E, Movie 5).

210 We further examined the ERK activity response to cell deformation. The manipulation of
211 cell shape in curved epithelial tissues remains unfeasible under 3D culture conditions; thus, we
212 performed a strain perturbation assay under planar culture conditions using dissociated lung
213 epithelial cells (Figure 3F). Under planar culture conditions, the stretching of cells led to ERK
214 activation, while their compression led to ERK inactivation (Figure 3G, 3H), indicating that
215 the strain on the cell area is key to curvature-dependent ERK activity regulation. Notably, the
216 surface area of the basal side of a cell is significantly larger in the convex region with high
217 ERK activity than in the concave region with lower ERK activity (Figure 2G). Together,
218 epithelial tissue curvature controls the ERK activity in cells, most likely through the strained
219 state of their basal membranes.

220

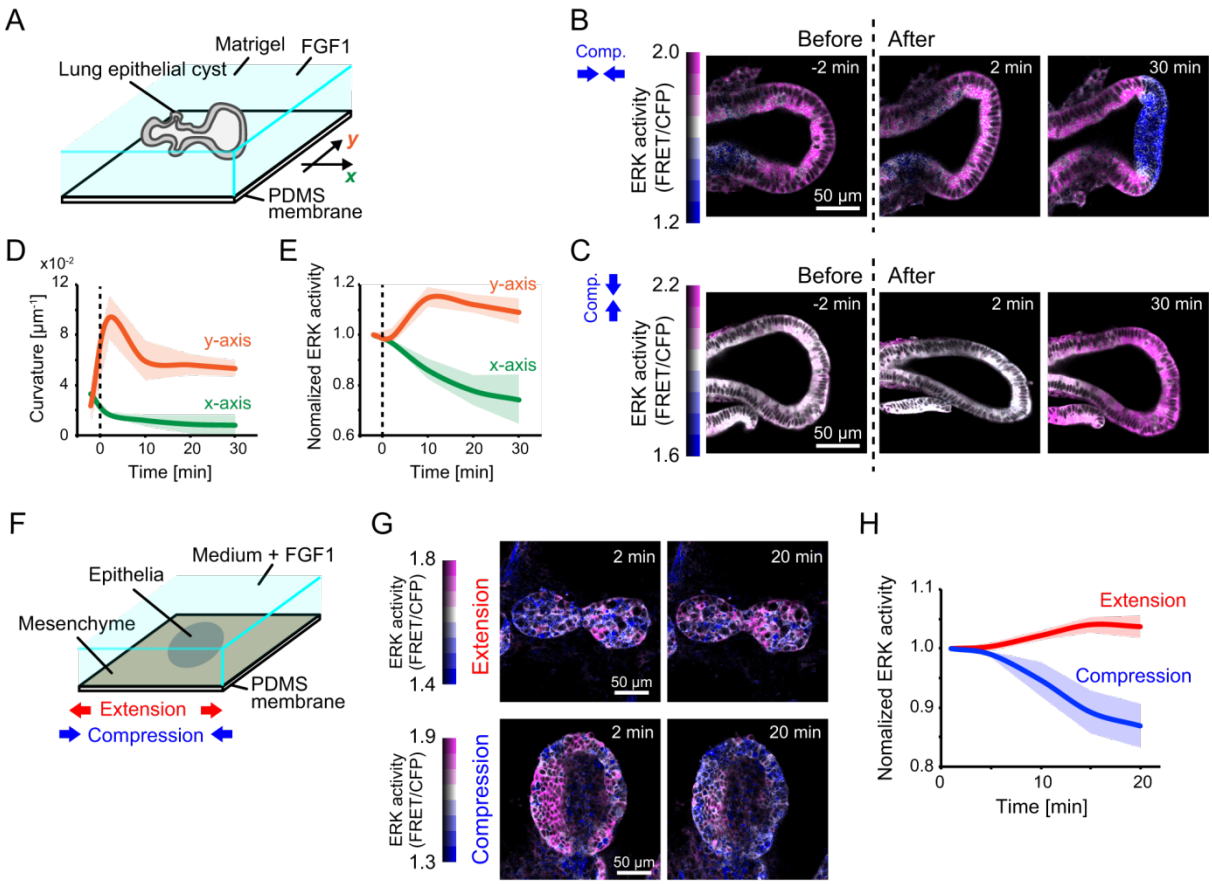

Figure 3 Response of ERK activity to mechanical perturbation

(A) Schematics of uniaxial compression assay performed on an isolated epithelium under 3D culture conditions. The *x* and *y* axes indicate directions parallel and vertical to the distal and proximal axes of the epithelium, respectively.

(B, C) Time-lapse images of the ERK activity for parallel compression (B) and vertical compression (C). Time origin indicates the timing of mechanical compression. Scale bars, 50 µm.

(D, E) Tissue curvature at the tip apex (D) and normalized ERK activity (E) over time. Colors represent the axes of compression, as shown in (A). Data represent mean and SD values. N=3.

(F) Schematics of uniaxial mechanical perturbations under 2D culture conditions.

(G) Time-lapse images of the ERK activity in the isolated lung epithelium for the extension (upper) and compression (lower) processes. Scale bar, 50 µm.

(H) Normalized ERK activity for the extension (red) and the compression (blue) processes over time. Time origin indicates the timing of mechanical perturbations. Data represent mean and SD values. N=3.

239 **4. ERK activation modulates cell shape via actin polymerization at the apical side**
240 Next, we investigate how the ERK activity contributes to epithelial morphology and mechanics.
241 First, we observed the change in the cell shape of isolated epithelial tissues treated with
242 PD0325901. Drug treatment led to an inhibition in the ERK activity within 30 min after
243 administration (Figure S3A), and the apico-basal length of epithelial cells became longer than
244 that observed in the control within 2 hours (Figure 4A, Movie 6). Hereafter, we refer to the
245 apico-basal length of cells as the cell height, and the cell length orthogonal to the apico-basal
246 axis as the cell width (Figure 4B). ERK inactivation in cells treated with PD0325901 lengthens
247 the cell height to 124% and shortens the cell width to 92% on an average, despite no significant
248 changes in the cell size, compared to mock-treated cells (Figure 4C). This trend is consistent
249 with that observed in the dissected murine lungs (Figure 1E–G). These results indicate that the
250 ERK activity regulates the cell height, while maintaining the cell size.
251 Next, to explore what causes the cell shape to change mechanically, we performed
252 inhibitor assays on cytoskeletons, such as actin, microtubule, and non-muscle myosin, which
253 allowed us to determine the mechanical contributions of targeted cytoskeletons to the cell
254 morphology. Given that the cell size is maintained even if the cell shape varies (Figure 4C),
255 two representative geometrical parameters, cell height and cell width, are in an inverse
256 relationship (see Materials and Methods IIa). Thus, we focused only on the change in the cell
257 height caused by cytoskeletal perturbations. The cell height was increased markedly upon
258 treatment with Latrunculin A or Cytochalasin D, each an inhibitor of actin polymerization, as
259 observed in inhibiting ERK activity with PD0325901; conversely, the cell height was
260 decreased by treatment with Jasplakinolide, which promotes actin polymerization (Figure 4D,
261 4E). Because F-actin remarkably accumulates at the apical side of cells (Figure S3B), we
262 speculated that actin polymerization at the apical edge would contribute to cell width extension,
263 leading to the shortening of the cell height. The cell height was also shortened by interfering
264 with microtubule polymerization with Nocodazole; combined treatment with Nocodazole and
265 Latrunculin A resulted in significant cell height extension via the rupture of lateral cell edges
266 (Figure S3D). Microtubules within cells are distributed along the apico-basal axis (Figure S3C),
267 and would thus stabilize cytoskeletal architectures sustaining cell height with F-actin. The
268 inhibition of the activity of non-muscle myosin II with Blebbistatin resulted in no significant
269 difference in cell height, compared to that observed with DMSO control (Figure 4E). This was
270 consistent with the fact that the activity of myosin is insignificant in the tips of lung epithelial
271 tissue (Figure S3E-E”). To further analyze the mode of actin polymerization, we used CK-666,
272 an Arp2/3 complex inhibitor CK-666, and SMIFH2, an inhibitor of the formin homology 2

domain. We found that the cell height was lengthened for CK-666 treatment, but slightly shortened for SMIFH2 treatment (Figure 4E), suggesting that actin polymerization would depend on the Arp2/3-mediated nucleation of branched filaments, rather than formin-mediated actin nucleation.

Because the inhibition of ERK activity and actin polymerization resulted in similar effects on the cell height, we speculated that ERK activation promoted F-actin accumulation within cells. Simultaneous imaging for the two factors revealed that F-actin accumulation at the apical side of cells was observed exclusively in the tips where ERK activation occurs, under FGF1-treated conditions (Figure 4F). Mapping between the ERK activity and F-actin accumulation level via 3D whole-tissue imaging clearly showed a positive correlation with FGF1 (ρ=0.51), although the inhibition of the ERK activity led to a significant decrease in F-actin accumulation at the apical side of cells throughout the tissue, and relatively uniform distribution (Figure 4G). In addition, treatment with FGF7, which activates ERK globally in the isolated epithelial tissues, regardless of the tissue curvature (Figure 2C), led to an increase in the apical F-actin accumulation overall throughout the epithelial tissues (Figure 4G). Thus, we found that ERK activation promotes actin polymerization at the apical edges of cells, and ultimately controls the cellular shape in the epithelial monolayer.

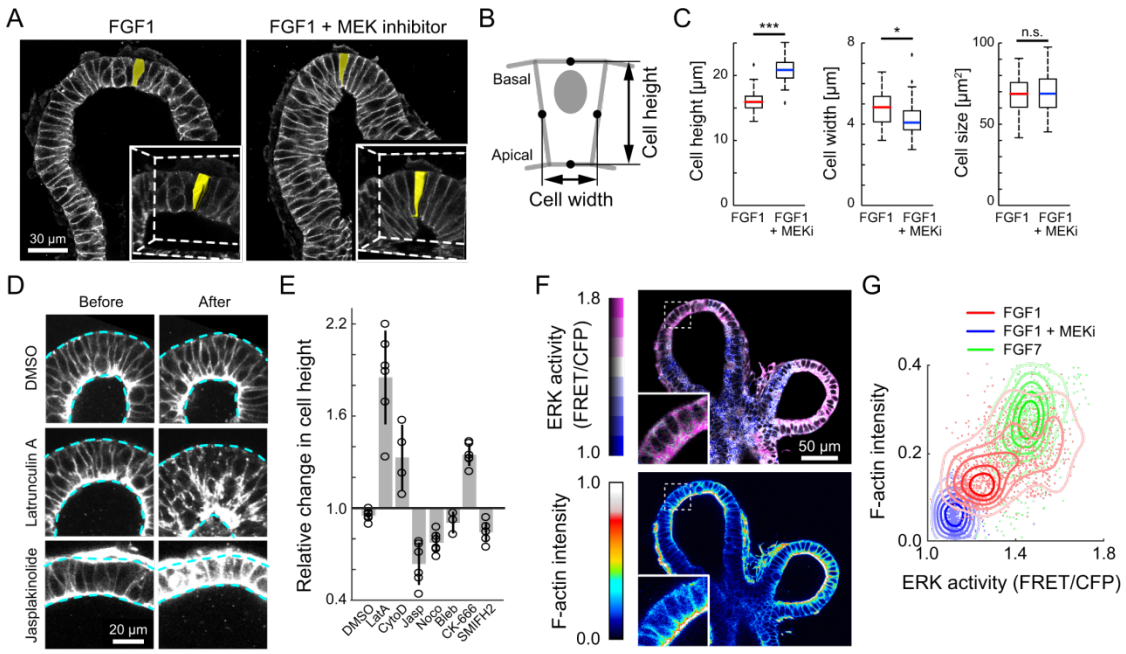

Figure 4 Response of cell morphology to chemical perturbations

(A) Change in the cell shape of an isolated epithelium upon treatment with either 500 ng mL^{-1} FGF1 (left) or 500 ng mL^{-1} FGF1 and 1 μM PD0325901. Cell membranes were visualized

using the whole-mount immunofluorescence of anti-E-cadherin. The inset windows represent a magnified 3D rendering focusing on a representative single cell marked in yellow. Scale bar, 30 μm.

(B) Schematics for cellular morphological measurement.

(C) Quantification of cell morphological parameters, including cell height, width, and size. n=60, N=3. Welch's t test, $p<0.001$ (left), $p=0.013$ (middle), and $p=0.4$ (right).

(D) Change in the cell morphology of an isolated epithelium upon treatment with either DMSO as a control, 1 μM Latrunculin A, or 1 μM Jasplakinolide. The cell shape was visualized using SiR-Actin, a F-actin labeling probe. Scale bar, 20 μm.

(E) Relative change in cell height upon inhibitor treatment for cytoskeletons. Concentrations of inhibitors: 1 μM Latrunculin A, 1 μM Cytochalasin D, 1 μM Nocodazole, 30 μM Blebbistatin, 1 μM Jasplakinolide, 100 μM CK-666, and 10 μM SMIFH2. The bar graph and error bars represent mean and SD values. $N\geq3$ for each treatment.

(F) Spatial map of ERK activity and F-actin accumulation level visualized by SiR-Actin labeling upon treatment with 500 ng mL^{-1} FGF1. Inset windows show magnified views that focus on their subcellular localization. Scale bar, 50 μm.

(G) Scatter plot and contour map of ERK activity in the cytosol and F-actin intensity at the apical edge. Colors indicate the administration of different chemicals; red: 500 ng mL^{-1} FGF1, n=1204, N=4, blue: 500 ng mL^{-1} FGF1 and 1 μM PD0325901 (MEKi), n=687, N=3, green: 100 ng mL^{-1} FGF7, n=787, N=3.

5. ERK activation flattens epithelial tissues via apical actin polymerization

How does the ERK-mediated actin polymerization at the apical side of cells result in morphological changes in monolayer tissues? To answer this, we used a simple geometrical model of a two-dimensional monolayer tissue, composed of cells with identical morphologies. In this model, individual cells are depicted by tetragons, the edges of which each correspond to the apical, basal, and lateral sides of cells. Then, the sheet curvature κ can be represented as a function of the length of these edges; especially, a change in the curvature with respect to the apical edge length a can be derived as $\partial\kappa/\partial a < 0$. Thus, the sheet curvature decreases with an expansion in the apical edge (see Materials and Methods IIb). This theoretical analysis predicts that ERK activation would decrease the tissue curvature via actin polymerization at the apical edges.

To confirm this prediction, we examined the change in epithelial tissue curvature in response to acute ERK activation. For this purpose, an isolated lung epithelium was incubated in the culture medium without any growth factors. Then, FGF1 was added into the medium to simulate ERK. Acute ERK activation exclusively promoted F-actin accumulation at the apical side of cells in epithelial distal tips; this was followed by the flattening of the epithelial sheet (Figure 5A–D, Movie 7). Moreover, the simultaneous administration of FGF1 and PD0325901 resulted in neither F-actin accumulation nor tip flattening; this was also observed for PBS control treatment (Figure 5B–D). These results indicate that ERK activation flattens the epithelial tissues in the tips via actin polymerization at the apical sides of cells.

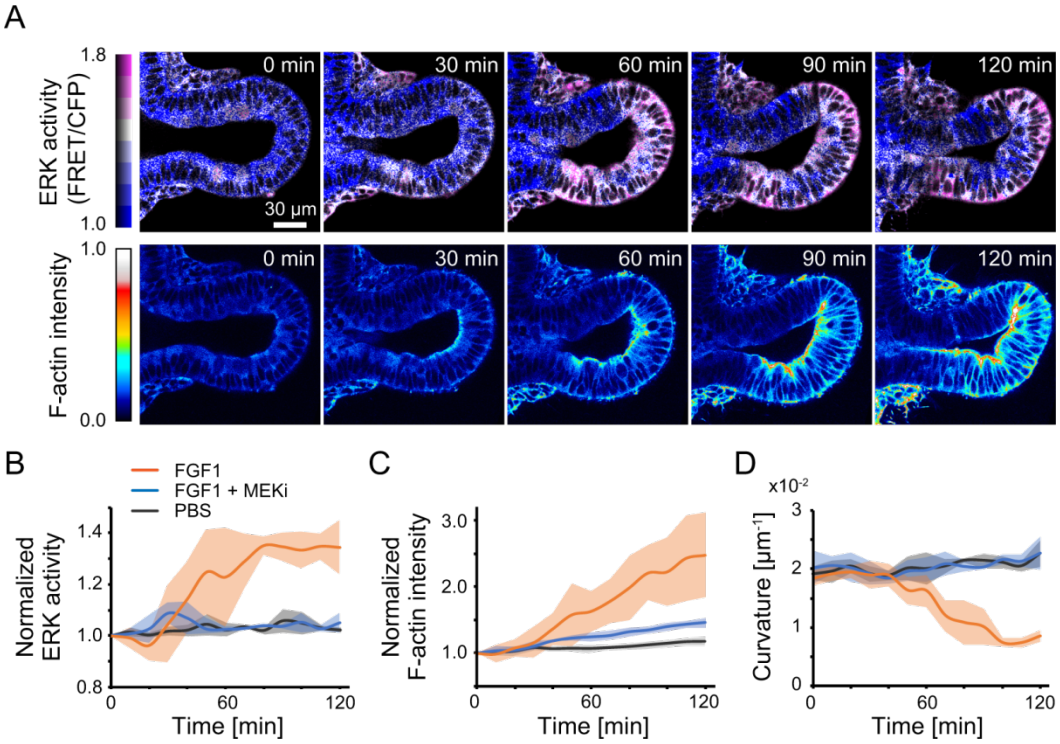

Figure 5 Simultaneous imaging of FGF-triggered ERK activation, actin polymerization, and tissue flattening

(A) Time-lapse images of ERK activity (upper) and F-actin intensity (lower). SiR-Actin was pretreated for F-actin visualization, 1 hour before the addition of FGF1. The time origin indicates the timing of FGF1 administration. Scale bar, 30 µm.

(B–D) Normalized ERK activity in the tips (B), normalized F-actin intensity in the tips (C), and tissue curvature at the tip apex (D) over time. Colors indicate different chemical treatments, including with 500 ng mL^{-1} FGF1 and 1 µM PD0325901 (MEKi). The time origin indicates the timing of chemical administration. Data represent mean and SD values. N=4.

6. Feedback between ERK activity and tissue curvature explains repetitive branching

To examine whether the curvature-dependent apical extension would be able to produce the periodic branching pattern, we performed numerical analysis using vertex dynamics model, a cell-based mechanical model [30–32]. The model represents epithelial cells as polygons with vertices and edges, and the edges on the apical side actively deform via F-actin dynamics that depend on the tissue-scale curvature and its decay (as described in Materials and Methods IIc). We conducted numerical simulations with an initial shape and bud diameters obtained from the experiment (Figure 6A), and examined the impact of curvature on the change in apical edge length through a model parameter α, using the standardized parameter set (Figure S4A). The apical edge extends/shrinks in accordance with the positive/negative values of α in a curvature-dependent manner (Figure 6B). Clearly, the curvature and cell height at the tip apex decreased with an increase in α at equilibrium (Figure 2B, S5B). Moreover, during curvature-dependent apical extension ($\alpha = 1$), the curvature decreases at the tip apex (arrowhead, Figure 2C), but increases at both sides over time (arrows, Figure 2C), indicating that the curvature-dependent apical extension can create new buds for terminal bifurcation. This does not happen in the opposite case ($\alpha = -1$), suggesting that curvature-dependent apical constriction is not likely to drive repetitive branching, contradictory to a previous report [33].

We then enabled cell proliferation to occur in the model system, in order to perform in silico experiments in virtual growing monolayer tissues. The simulation of the regime of curvature-dependent apical extension and cell proliferation clearly demonstrates the formation of repetitive branching patterns (Figure 6D, Movie 8). In contrast, the repetitive branching pattern is not generated in counterpart regimes, such as no regulation on the apical edge, and global apical extension as observed for the FGF7 treatment – apical extension happens in all cells, irrespective of curvature (Figure 6E). In these counterpart regimes, there are significant differences in both the averaged curvature, a measure of curvature averaged over the entire tissue, and the correlation coefficient between the curvature and monolayer thickness (Figure 6F, 6G). Moreover, the virtual experiments show that luminal pressure, which has been proposed to be a physical factor for lung morphogenesis [34,35], is not essential for branching pattern formation; rather, it suppresses its constant large magnitude value (Figure S4C). These results support the fact that that the exclusive occurrence of apical edge extension in cells with high curvatures drives repetitive terminal bifurcation in the growing epithelial monolayer in a self-sustaining manner.

Furthermore, numerical investigations have clarified that the retention time of curvature memory in F-actin, i.e., the inverse of the F-actin decay rate γ, is crucial for generating the

branching pattern (Figure 6H, Movie 9–11). The averaged curvature becomes larger for a longer curvature memory, and the correlation between the curvature and F-actin becomes higher for a shorter curvature memory. Thus, there is an optimal range for the retention time of the curvature memory in F-actin (Figure 6I). This result suggests the importance of the tissue curvature hysteresis of cellular force generation via F-actin, for the emergence of repetitive branch patterns.

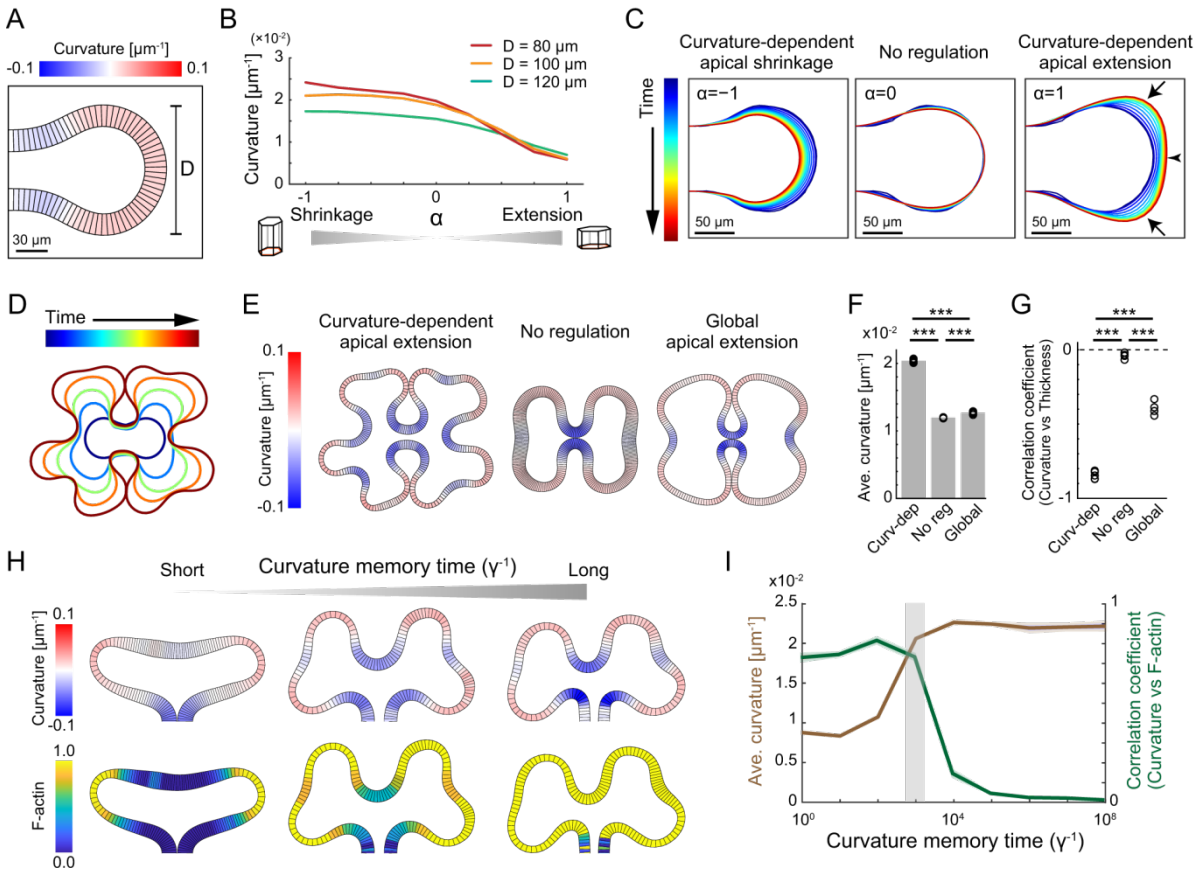

Figure 6 Simulation and analysis of the mathematical model

(A) Distal tip of a virtual epithelial monolayer tissue during the initial configuration of the simulation. Colors indicate the tissue curvature. D represents the diameter of the tip. Scale bar, 30 μm.

(B) Tissue curvature at the tip apex over the parameter α. Colors indicate the tip diameter.

(C) Time evolution of the basal sides of cells in different α. Colors indicate the time periods in simulations. The arrowhead indicates the tip apex and arrows indicate the regions with a growing curvature. Scale bars, 50 μm.

(D) Time evolution of the basal sides of cells in the simulation with cell proliferation at α=1.

(E) Generated morphology of epithelial monolayer tissues in different regimes. Curvature-dependent apical extension: α=1, β=0; no regulation: α=0, β=0; global apical extension: α=0, β=0.2.

(F, G) Averaged curvature (F) and correlation coefficient between the tissue curvature and tissue thickness (G) for the 3 regulatory regimes. Bars represent mean values. N=5. Welch's t-test, $p<0.001$.

(H) Spatial maps of the curvature (upper) and F-actin level (lower) for different curvature memory time periods γ^{-1}. left: $\gamma=1$, middle: $\gamma= 10^{-3}$, right: $\gamma= 10^{-6}$.

(I) Tissue curvature (green) and correlation coefficient between the curvature and the F-actin level. Data represent mean and SD values. N=5. The gray shaded region indicates the region in which both the values are high.

Discussion

Here, we have demonstrated a regulatory mechanism by which epithelial monolayer cells undergo repetitive branching morphogenesis through curvature sensing and ERK-mediated mechanical force generation in a self-sustained manner. Our two-photon live imaging analysis has shown that the ERK activity changes following a dynamic change in the tissue curvature, and ERK activation occurs preferentially in curved epithelial tissues. Moreover, we found that ERK-mediated actin polymerization contributes to the extension of the apical side of cells, and demonstrated its importance for achieving a decrease in tissue curvature during terminal bifurcation via mathematical model analyses. Thus, there is a closed negative feedback loop between the tissue curvature and ERK activity across multiple scales in developing lung epithelial tissues (Figure 7).

The results presented in this study provide a better understanding of lung epithelial branching, in conjunction with previously determined theory-based mechanisms, based on mechanical and chemical aspects. From a mechanical viewpoint, it has been proposed that the spatial patterning of the isolated lung epithelium arises from the proliferation-induced physical instability of the epithelial layer, known as mechanical buckling [36], in various developing epithelial tissues [1,37,38]. This purely mechanical model may explain the formation of an initial branching pattern, under the assumption that the epithelial tissue acts as an elastic layer, but may require the physical conditions under which mechanical buckling occurs. However, our results have demonstrated that repetitive branching can be generated even at a range where proliferation-induced buckling did not occur (Figure 6E–G). We emphasize that the regime presented here is not mutually exclusive to buckling-induced patterning. Thus, ERK-mediated tissue curvature feedback results in a robust regulatory system underlying branching morphogenesis, together with the buckling regime. In addition, a simple reaction–diffusion model of substrate–depletion has been proposed for integrating chemical signal and tissue growth [39,40]; the model assumes that lung epithelial cells consume FGF ligands that have slow diffusion rates, and thereby predicts that a concentration gradient of FGF is generated in the extracellular matrix. However, live imaging analysis results have shown that no FGF gradient was formed in the Matrigel, while FGF was internalized in the epithelial cells through endocytosis (Figure S2). Other reaction-diffusion systems have focused on genetic regulatory networks that can achieve the localization of *Fgf10* expression observed in vivo [41–43]. Although the spatial distribution of the chemoattractant is dispensable for epithelial branching [18] (Figure 2D), the incorporation of such fundamental biochemical signals into our model would be useful for studying detailed systems for lung branching and patterning in vivo.

Our findings highlight the curvature-sensitive ERK activation of lung epithelial cells and raise an important question about how cells sense the tissue curvature and transmit FGF–ERK signals. Because the ERK activity response occurs within 10 min after the perturbation in the tissue curvature (Figure 3B–E), the chemical feedbacks via gene expression, e.g., the interplay between the FGF and Sonic hedgehog expressed in the epithelium, are unlikely but rather via unknown protein–protein interactions should be involved in this process. We determined from the results (Figure 2G, 3G–H) that the phenomenon of curvature-sensitive ERK activation in lung epithelial tissues was attributable to a strain exhibiting a certain cell membrane or level of membrane tension, as shown previously for other tissues [44–46]. Moreover, the state of the membrane would trigger receptor-mediated endocytosis, as FGF internalization occurs exclusively in epithelial tissues with a positive curvature (Figure S2). Multiple intracellular events, including the endocytic trafficking of FGFR and molecular sensing of plasma membrane curvature, would be involved in this process [47–49].

This study has focused on the core mechanism to minimally generate the self-sustained repetitive branching patterns in epithelium; however, there are other additional contributions that could achieve the robust tissue morphogenesis in vivo. For example, smooth muscle cells are not necessary for the initiation of cleft formation (Figure 2D)[50], but should mechanically assist the cleft formation from the outside of an epithelium, realizing the stable terminal bifurcation [27,50]. Luminal fluid is another potentially important factor that can mechanically affect epithelial tissue deformation through shear stress and hydrostatic pressure [51]. It has been previously reported that the manipulation of luminal pressure in murine developing lungs under ex vivo culture conditions altered branch formation [34]. As oscillatory contractions of airway smooth muscles are likely to produce dynamic changes in the luminal pressure, it has been suggested that rhythmic luminal pressure would control the global synchronization of branching events in the murine lung [35], although it does not contribute to the tissue flattening during the terminal bifurcation.

The ERK-mediated curvature feedback mechanism proposed here advances the concept of mechanochemical regulation of the epithelial monolayer [32,44,52,53], in terms of taking the impact of tissue geometry into account. In various tissues, the epithelial cells collectively form their shape in the tissue scale and the constituent cells respond to tissue curvature at different levels, including the transcription and cell activity levels [54–57]. We believe that the proposed system works as a regulatory principle underlying the mechanisms of self-organized tissue morphogenesis.

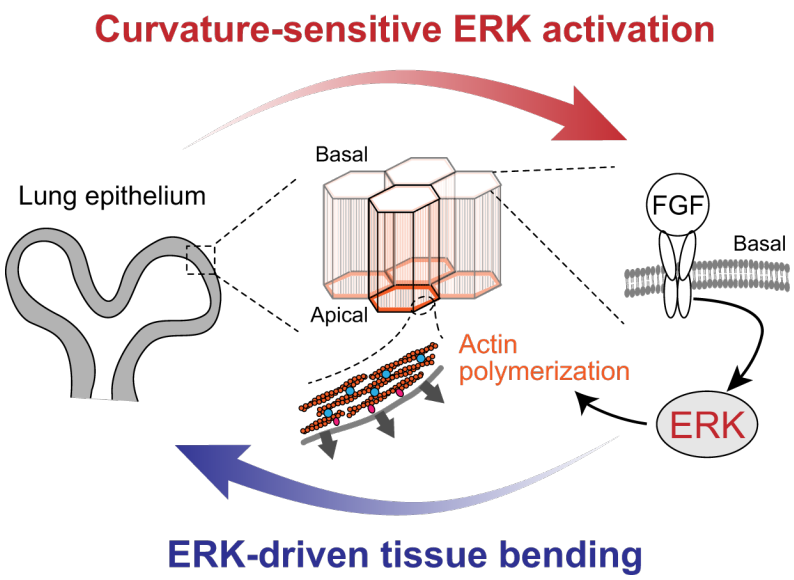

Figure 7 ERK-mediated curvature feedback regulates branching morphogenesis in murine lung epithelial tissue

The epithelial cells activate ERK specifically in tissues with a positive curvature via reception of extracellular FGF ligands (red arrow). ERK-mediated actin polymerization contributes to the extension of the apical side of cells, which decreases the tissue curvature (blue arrow). Thus, there is a closed negative feedback loop between tissue curvature and ERK activity across multiple scales in developing epithelial lung tissues.

Acknowledgements

This work was supported by the JST PRESTO grant JPMJPR1949, by the JSPS KAKENHI 19H00993, by the SPIRITS 2018 of Kyoto University, and by the Medical Research Support Center of Kyoto University. We would like to thank Akane Kusumi for technical assistance, Edouard Hannezo, Naoya Hino, Mamoru Ishii, and Takuya Yoshida for fruitful discussion.

Author Contributions

Conceptualization, T.H.; Methodology, T.H.; Software, T.H.; Validation, T.H.; Formal analysis, T.H.; Investigation, T.H.; Resources, T.H., M.M.; Data curation, T.H.; Writing - original draft, T.H.; Writing - review & editing, T.H., M.M.; Visualization, T.H.; Supervision, T.H.; Project administration, T.H., M.M.; Funding acquisition, T.H., M.M.

Competing interests

The authors declare no competing interests.

509 **References**

510 1. Hirashima, T. Pattern Formation of an Epithelial Tubule by Mechanical Instability
511 during Epididymal Development. *Cell Rep.* **9**, 866–73 (2014).
512 2. Metzger, R. J., Klein, O. D., Martin, G. R. & Krasnow, M. A. The branching
513 programme of mouse lung development. *Nature* **453**, 745–750 (2008).
514 3. Hannezo, E. *et al.* A Unifying Theory of Branching Morphogenesis. *Cell* (2017).
515 doi:10.1016/j.cell.2017.08.026
516 4. Lu, P. & Werb, Z. Patterning mechanisms of branched organs. *Science (80-.).* **322**,
517 1506–1509 (2008).
518 5. Cardoso, W. V. & Lü, J. Regulation of early lung morphogenesis: questions, facts and
519 controversies. *Development* **133**, 1611–1624 (2006).
520 6. Warburton, D. *et al.* Lung organogenesis. in *Current Topics in Developmental Biology*
521 (2010). doi:10.1016/S0070-2153(10)90003-3
522 7. Herriges, M. & Morrisey, E. E. Lung development: Orchestrating the generation and
523 regeneration of a complex organ. *Development (Cambridge)* (2014).
524 doi:10.1242/dev.098186
525 8. Varner, V. D. & Nelson, C. M. Cellular and physical mechanisms of branching
526 morphogenesis. *Development* **141**, 2750–9 (2014).
527 9. Ingber, D. E. Mechanical control of tissue morphogenesis during embryological
528 development. *Int. J. Dev. Biol.* (2006). doi:10.1387/ijdb.052044di
529 10. Anlaş, A. A. & Nelson, C. M. Tissue mechanics regulates form, function, and
530 dysfunction. *Current Opinion in Cell Biology* (2018). doi:10.1016/j.ceb.2018.05.012
531 11. Ornitz, D. M. & Itoh, N. The Fibroblast Growth Factor signaling pathway. *Wiley*
532 *Interdiscip. Rev. Dev. Biol.* **4**, 215–266 (2015).
533 12. Cardoso, W. V., Itoh, A., Nogawa, H., Mason, I. & Brody, J. S. FGF-1 and FGF-7
534 induce distinct patterns of growth and differentiation in embryonic lung epithelium.
535 *Dev. Dyn.* (1997). doi:10.1002/(SICI)1097-0177(199703)208:3<398::AID-
536 AJA10>3.0.CO;2-X
537 13. Nogawa, H. & Ito, T. Branching morphogenesis of embryonic mouse lung epithelium
538 in mesenchyme-free culture. *Development* (1995).
539 14. Bellusci, S., Grindley, J., Emoto, H., Itoh, N. & Hogan, B. L. M. Fibroblast Growth
540 Factor 10 (FGF10) and branching morphogenesis in the embryonic mouse lung.
541 *Development* (1997).
542 15. Min, H. *et al.* Fgf-10 is required for both limb and lung development and exhibits

543 striking functional similarity to Drosophila branchless. *Genes Dev.* (1998).
544 doi:10.1101/gad.12.20.3156
545 16. Sekine, K. *et al.* Fgf10 is essential for limb and lung formation. *Nat. Genet.* (1999).
546 doi:10.1038/5096
547 17. Arman, E., Haffner-Krausz, R., Gorivodsky, M. & Lonai, P. Fgfr2 is required for limb
548 outgrowth and lung-branching morphogenesis. *Proc. Natl. Acad. Sci. U. S. A.* (1999).
549 doi:10.1073/pnas.96.21.11895
550 18. Volckaert, T. *et al.* Localized Fgf10 expression is not required for lung branching
551 morphogenesis but prevents differentiation of epithelial progenitors. *Dev.* (2013).
552 doi:10.1242/dev.096560
553 19. Boucherat, O., Nadeau, V., Berube-Simard, F.-A., Charron, J. & Jeannotte, L. Crucial
554 requirement of ERK/MAPK signaling in respiratory tract development. *Development*
555 **142**, 3801–3801 (2015).
556 20. Yoshida, T., Matsuda, M. & Hirashima, T. Incoherent Feedforward Regulation via
557 Sox9 and ERK Underpins Mouse Tracheal Cartilage Development. *Front. Cell Dev.*
558 *Biol.* **8**, (2020).
559 21. Liu, Y. *et al.* Novel role for netrins in regulating epithelial behavior during lung
560 branching morphogenesis. *Curr. Biol.* (2004). doi:10.1016/j.cub.2004.05.020
561 22. Jiang, K., Tang, Z., Li, J., Wang, F. & Tang, N. Anxa4 mediated airway progenitor
562 cell migration promotes distal epithelial cell fate specification. *Sci. Rep.* (2018).
563 doi:10.1038/s41598-018-32494-z
564 23. Tang, N., Marshall, W. F., McMahon, M., Metzger, R. J. & Martin, G. R. Control of
565 Mitotic Spindle Angle by the RAS-Regulated ERK1/2 Pathway Determines Lung
566 Tube Shape. *Science (80-.).* **333**, 342–345 (2011).
567 24. Komatsu, N. *et al.* A platform of BRET-FRET hybrid biosensors for optogenetics,
568 chemical screening, and in vivo imaging. *Sci. Rep.* **8**, 8984 (2018).
569 25. Komatsu, N. *et al.* Development of an optimized backbone of FRET biosensors for
570 kinases and GTPases. *Mol. Biol. Cell* **22**, 4647–56 (2011).
571 26. Harvey, C. D. *et al.* A genetically encoded fluorescent sensor of ERK activity. *Proc.*
572 *Natl. Acad. Sci. U. S. A.* **105**, 19264–9 (2008).
573 27. Kim, H. Y. *et al.* Localized Smooth Muscle Differentiation Is Essential for Epithelial
574 Bifurcation during Branching Morphogenesis of the Mammalian Lung. *Dev. Cell*
575 (2015). doi:10.1016/j.devcel.2015.08.012
576 28. Yuan, T. *et al.* Temporospatial Expression of Fgfr1 and 2 During Lung Development,

577 Homeostasis, and Regeneration. *Front. Pharmacol.* **11**, (2020).
578 29. De Moerlooze, L. *et al.* An important role for the IIIb isoform of fibroblast growth
579 factor receptor 2 (FGFR2) in mesenchymal-epithelial signalling during mouse
580 organogenesis. *Development* **127**, 483–492 (2000).
581 30. Fletcher, A. G., Osterfield, M., Baker, R. E. & Shvartsman, S. Y. Vertex models of
582 epithelial morphogenesis. *Biophys. J.* **106**, 2291–2304 (2014).
583 31. Nagai, T. & Honda, H. A dynamic cell model for the formation of epithelial tissues.
584 *Philos. Mag. B* **81**, 699–719 (2001).
585 32. Hirashima, T. & Adachi, T. Polarized cellular mechano-response system for
586 maintaining radial size in developing epithelial tubes. *Development* **146**, dev181206
587 (2019).
588 33. Fumoto, K., Takigawa-Imamura, H., Sumiyama, K., Kaneiwa, T. & Kikuchi, A.
589 Modulation of apical constriction by Wnt signaling is required for lung epithelial
590 shape transition. *Development* **144**, 151–162 (2017).
591 34. Unbekandt, M. *et al.* Tracheal occlusion increases the rate of epithelial branching of
592 embryonic mouse lung via the FGF10-FGFR2b-Sprouty2 pathway. *Mech. Dev.* **125**,
593 314–324 (2008).
594 35. Nelson, C. M. *et al.* Microfluidic chest cavities reveal that transmural pressure controls
595 the rate of lung development. *Development* (2017). doi:10.1242/dev.154823
596 36. Varner, V. D., Gleghorn, J. P., Miller, E., Radisky, D. C. & Nelson, C. M.
597 Mechanically patterning the embryonic airway epithelium. *Proc. Natl. Acad. Sci.* **112**,
598 9230–9235 (2015).
599 37. Kourouklis, A. P. & Nelson, C. M. Modeling branching morphogenesis using
600 materials with programmable mechanical instabilities. *Curr. Opin. Biomed. Eng.* **6**,
601 66–73 (2018).
602 38. Savin, T. *et al.* On the growth and form of the gut. *Nature* **476**, 57–62 (2011).
603 39. Miura, T. & Shiota, K. Depletion of FGF acts as a lateral inhibitory factor in lung
604 branching morphogenesis in vitro. *Mech. Dev.* **116**, 29–38 (2002).
605 40. Hartmann, D. & Miura, T. Modelling in vitro lung branching morphogenesis during
606 development. *J. Theor. Biol.* **242**, 862–872 (2006).
607 41. Hirashima, T., Iwasa, Y. & Morishita, Y. Mechanisms for split localization of Fgf10
608 expression in early lung development. *Dev. Dyn.* **238**, 2813–2822 (2009).
609 42. Menshykau, D., Kraemer, C. & Iber, D. Branch Mode Selection during Early Lung
610 Development. *PLoS Comput. Biol.* **8**, e1002377 (2012).

611 43. Menshykau, D., Blanc, P., Unal, E., Sapin, V. & Iber, D. An interplay of geometry and
612 signaling enables robust lung branching morphogenesis. *Development* **141**, 4526–4536
613 (2014).
614 44. Hino, N. *et al.* ERK-Mediated Mechanochemical Waves Direct Collective Cell
615 Polarization. *Dev. Cell* **53**, 646-660.e8 (2020).
616 45. Kinoshita, N. *et al.* Mechanical Stress Regulates Epithelial Tissue Integrity and
617 Stiffness through the FGFR/Erk2 Signaling Pathway during Embryogenesis. *Cell Rep.*
618 **30**, 3875-3888.e3 (2020).
619 46. Sitarska, E. & Diz-Muñoz, A. Pay attention to membrane tension: Mechanobiology of
620 the cell surface. *Curr. Opin. Cell Biol.* **66**, 11–18 (2020).
621 47. Francavilla, C. *et al.* Functional Proteomics Defines the Molecular Switch Underlying
622 FGF Receptor Trafficking and Cellular Outputs. *Mol. Cell* **51**, 707–722 (2013).
623 48. Belleudi, F. *et al.* Keratinocyte Growth Factor Receptor Ligands Target the Receptor
624 to Different Intracellular Pathways. *Traffic* **8**, 1854–1872 (2007).
625 49. Antonny, B. Mechanisms of Membrane Curvature Sensing. *Annu. Rev. Biochem.* **80**,
626 101–123 (2011).
627 50. Young, R. E. *et al.* Airway Smooth Muscle Differentiation is Essential for Promoting
628 Airway Size, Tracheal Cartilage Segmentation, But Dispensable for Epithelial
629 Branching. *SSRN Electron. J.* (2019). doi:10.2139/ssrn.3454659
630 51. Chan, C. J. & Hiiragi, T. Integration of luminal pressure and signalling in tissue self-
631 organization. *Development* **147**, dev181297 (2020).
632 52. Boocock, D., Hino, N., Ruzickova, N., Hirashima, T. & Hannezo, E. Theory of
633 mechanochemical patterning and optimal migration in cell monolayers. *Nat. Phys.* **17**,
634 267–274 (2021).
635 53. Ishii, M., Tateya, T., Matsuda, M. & Hirashima, T. Retrograde ERK activation waves
636 drive base-to-apex multicellular flow in murine cochlear duct morphogenesis. *Elife* **10**,
637 (2021).
638 54. Nikolaev, M. *et al.* Homeostatic mini-intestines through scaffold-guided organoid
639 morphogenesis. *Nature* **585**, 574–578 (2020).
640 55. Nelson, C. M., VanDuijn, M. M., Inman, J. L., Fletcher, D. A. & Bissell, M. J. Tissue
641 Geometry Determines Sites of Mammary Branching Morphogenesis in Organotypic
642 Cultures. *Science (80-.).* **314**, 298–300 (2006).
643 56. Luciano, M. *et al.* Large-scale curvature sensing by epithelial monolayers depends on
644 active cell mechanics and nuclear mechanoadaptation. *bioRxiv* (2020).

645 doi:doi.org/10.1101/2020.07.04.187468
646 57. Hughes, A. J. *et al.* Engineered Tissue Folding by Mechanical Compaction of the
647 Mesenchyme. *Dev. Cell* **44**, 165-178.e6 (2018).
648 58. Hirashima, T. & Adachi, T. Procedures for the Quantification of Whole-Tissue
649 Immunofluorescence Images Obtained at Single-Cell Resolution during Murine
650 Tubular Organ Development. *PLoS One* **10**, e0135343 (2015).
651 59. Hirashima, T. Mechanical Tissue Compression and Whole-mount Imaging at Single
652 Cell Resolution for Developing Murine Epididymal Tubules. *BIO-PROTOCOL* **10**,
653 (2020).
654 60. Lukinavičius, G. *et al.* Fluorogenic probes for live-cell imaging of the cytoskeleton.
655 *Nat. Methods* (2014). doi:10.1038/nmeth.2972
656 61. Milroy, L. G. *et al.* Selective chemical imaging of static actin in live cells. *J. Am.*
657 *Chem. Soc.* (2012). doi:10.1021/ja211708z
658 62. Tran, A. P., Yan, S. & Fang, Q. Improving model-based functional near-infrared
659 spectroscopy analysis using mesh-based anatomical and light-transport models.
660 *Neurophotonics* **7**, 1 (2020).
661 63. Meyer, M., Desbrun, M., Schr, P. & Barr, A. H. Discrete Differential-Geometry
662 Operators for Triangulated 2-Manifolds. *Vis. Math. III* 113–134 (2003).
663 doi:10.1016/j.cagd.2007.07.005
664 64. Hannezo, E., Prost, J. & Joanny, J.-F. Theory of epithelial sheet morphology in three
665 dimensions. *Proc. Natl. Acad. Sci.* **111**, 27–32 (2014).
666 65. Wen, F. L., Wang, Y. C. & Shibata, T. Epithelial Folding Driven by Apical or Basal-
667 Lateral Modulation: Geometric Features, Mechanical Inference, and Boundary Effects.
668 *Biophys. J.* (2017). doi:10.1016/j.bpj.2017.05.012
669 66. Boucherat, O., Nadeau, V., Berube-Simard, F.-A., Charron, J. & Jeannotte, L. Crucial
670 requirement of ERK/MAPK signaling in respiratory tract development. *Development*
671 **142**, 3197–3211 (2014).
672
673

674 **Materials and Methods**

675 **(I) Experiments**

676 **Animals**

677 It has been previously reported that transgenic mice expressed hyBRET-ERK-NES, a FRET
678 biosensor [24–26]. hyBRET-ERK-NES is comprised of cyan fluorescent protein (CFP) and yellow
679 fluorescent protein (YFP), which act as the donor and acceptor of FRET, respectively.
680 Otherwise, we used ICR mice purchased from Japan SLC, Inc. We designated the midnight
681 preceding the discovery of the vaginal plug as embryonic day 0.0 (E0.0), and all mice were
682 sacrificed via cervical dislocation to minimize suffering. All animal experiments were
683 approved by the local ethical committee for animal experimentation (MedKyo 18086, 19090,
684 and 20081), and were performed in compliance with the guidelines for the care and use of
685 laboratory animals, at Kyoto University.

686

687 **Antibodies, small molecules, and recombinant proteins**

688 We used the following primary antibodies at a dilution ratio of 1:200 unless stated otherwise:
689 rat monoclonal anti-E-cadherin (Cell Signaling Technology, #3195), rabbit polyclonal anti-
690 phospho-myosin light chain (pMLC) (Abcam, #ab2480), Alexa Fluor 546-conjugated goat
691 anti-rat IgG (H+L) antibody (Thermo Fisher Scientific, #A11081, 1:1000), Alexa Fluor 647-
692 conjugated goat anti-rabbit IgG (H+L) antibody (Abcam, #ab150079, or Thermo Fisher
693 Scientific, #A21247, 1:1000), Blebbistatin (Merck Millipore, #203391), CK-666 (Sigma-
694 Aldrich, #SML0006), Cytochalasin D (Merck Millipore, #250255), FGF1 (R&D Systems,
695 #232-FA), FGF7 (R&D Systems, #251-KG), Jasplakinolide (Abcam, #ab141409), Latrunculin
696 A (Cayman Chemical, #10010630), Nocodazole (Merck Millipore, #487928), PD0325901
697 (FUJIFILM Wako Pure Chemical Corporation, #162-25291), SMIFH2 (Sigma-Aldrich,
698 #S4826), Y-27632 (Merck Millipore, #SCM075).

699

700 **Ex vivo culture**

701 Dissected lung lobes were placed onto a hydrophilic polytetrafluoroethylene organ culture
702 insert with a pore size of 0.4 μm (Merck Millipore, #PICM01250), which was preset in a 35
703 mm petri dish filled with 800 μL of culture medium. Samples were cultured in an air-liquid
704 interface at 37°C under 5% CO_2 conditions. To culture isolated epithelial tissues, dissected
705 lobes were digested with 10 PU/mL of Dispase I (FUJIFILM Wako Pure Chemical Corporation,
706 #386-02271) in phosphate buffered saline (PBS) for 15 min on ice, and immersed into fetal
707 bovine serum (FBS) and kept on ice for 5 min, to stop the protease-mediated reaction. Then,

708 samples were washed in PBS twice on ice, and the distal tips of epithelial tissues were manually
709 excised using fine needles. Isolated epithelial tissues were cultured within growth factor-
710 reduced Matrigel (Corning, #356231) and covered with 500 μL of culture medium added to
711 each well of glass bottom dishes (Greiner, #627870) at 37°C under 5% CO_2 conditions. We
712 used FluoroBrite DMEM Media (Thermo Fischer Scientific, #A1896701) containing 1%
713 GlutaMAX (Thermo Fischer Scientific, #35050061) and 0.5% FBS as the culture medium.
714
715 **Whole-tissue immune-fluorescence staining**
716 Staining and optical clearing of dissected lung were performed according to previous studies
717 [58,59]. Briefly, samples were fixed with 4% paraformaldehyde (PFA) in PBS overnight at 4°C.
718 For pMLC staining, samples were fixed with 2% trichloroacetic acid in PBS containing a 1%
719 phosphatase inhibitor cocktail (1:100, Nacalai Tesque, #07575-51) for 15 min at 4°C. Then,
720 samples were blocked by incubation in 10% normal goat serum (Abcam, #ab156046) diluted
721 in 0.1% Triton X-100/PBS (PBT) for 3 h at 37°C. Samples were treated with primary
722 antibodies overnight at 4°C, washed in 0.1% PBT, and subsequently treated with secondary
723 antibodies conjugated to either Alexa Fluor 546 or Alexa Fluor 647 overnight at 4°C. For
724 nuclear counterstaining, we used Hoechst33342 (5 μg/ml, Dojindo Molecular Technologies,
725 #H342) or DAPI (Dojindo Molecular Technologies, #D523-10, 1:200). The samples were
726 mounted with 10 μL of 1% agarose gel onto a glass-based dish (Greiner Bio-One, #627871)
727 for obtaining stable images. Then, samples were immersed with CUBIC-R+ (Tokyo Chemical
728 Industry Co., # T3741) solution for 1 hour at 37°C or BABB solution (benzyl-alcohol and
729 benzyl-benzoate, 1:2) for 30 min at 23°C.
730
731 **F-actin and tubulin labeling**
732 To visualize F-actin and microtubules, we used SiR-Actin and SiR-tubulin, respectively [60,61],
733 according to the manufacturer's instructions (Cytoskeleton, Inc. #CY-SC001 and #CY-SC002).
734 We added 1 μM of far-red fluorogenic probes to the culture media, 1 hour before imaging.
735 Although SiR-Actin was derived from Jasplakinolide, which activated ERK in isolated lung
736 epithelial tissues in our experiments, ERK activation did not occur after treatment with SiR-
737 Actin in isolated lung epithelial tissues.
738
739 **Fluorescence labeling of FGF**
740 To visualizes internalized FGFs, we used an amine-reactive pH-sensitive pHrodo iFL Red STP
741 ester dye, according to the manufacturer's instructions (Thermo Fischer Scientific, #P36014).

742 For the imaging of FGF1, regardless of its localization inside or outside cells, we used the
743 Alexa Fluor 488 Microscale Protein Labeling Kit, according to the manufacturer's instructions
744 (Thermo Fischer Scientific, #A30006).
745
746 **Microscopy**
747 For live imaging, we used the incubator-integrated multiphoton fluorescence microscope
748 system (LCV-MPE, Olympus) with a 25× water-immersion lens (NA=1.05, WD=2 mm,
749 XLPLN25XWMP2, Olympus) or an inverted microscope (FV1200MPE-IX83, Olympus) with
750 a 30× silicone-immersion lens (NA=1.05, WD=0.8 mm, UPLSAPO30XS, Olympus). The
751 excitation wavelengths were set to 840 nm for the CFP of the ERK FRET biosensor, 930 nm
752 for Alexa Fluor 488-labeled FGF1, and 1040 nm for the pHrodo iFL Red-labeled FGFs and
753 the SiR probes (InSight DeepSee, Spectra-Physics). We used RDM690 IR cut filters (Olympus),
754 and the DM505 and DM570 dichroic mirrors. We used BA460-500, BA495-540, BA520-560,
755 BA575-630, and BA647/57 emission filters (Olympus) for CFP, Alexa Fluor 488, YFP or
756 FRET, iFL Red probes, and SiR probes, respectively. For fixed samples, images were obtained
757 using the Leica TCS SP8 confocal laser scanning platform equipped with the Leica HyD hybrid
758 detector, using the 20× objective lens (NA=0.75, WD=680 μm, HC PL APO CS2, Leica) and
759 40× objective lens (NA = 1.3, WD = 240 μm, HC PL APO CS2, Leica).
760
761 **FRET image analysis**
762 The median filter of a 3 × 3 window was processed to remove shot noise, and the background
763 signal was subtracted from each FRET and CFP channel. Then, the ratio of FRET intensity to
764 CFP intensity was calculated using a custom-made MATLAB (MathWorks) script. In the scale
765 bar, the color represents the FRET/CFP ratio and brightness represents the fluorescence
766 intensity of the FRET channel.
767
768 **Three-dimensional mapping of different quantities**
769 To determine the correlation between different quantities, such as ERK activity, F-actin signal,
770 tissue curvature, and tissue thickness (Figure S1A), we obtained 3D stacked images of lung
771 epithelial tissues with 1-μm-long z-intervals, and manually traced either the basal or apical side
772 of the cells. Next, we generated triangle meshes on the traced surface using "Iso2Mesh," a free
773 mesh generation toolbox [62]. Then, we calculated a discrete Gaussian curvature and a discrete
774 curvature on each node of generated meshes using a custom-made code according to the
775 definition proposed earlier [63]. Finally, we obtained all values except those for the curvatures

776 by averaging values around the nodes, and mapped them at each node. All processing was
777 performed using MATLAB.
778
779 **Curvature measurement in 2D**
780 We used a spline curve-based method described elsewhere [53]. Briefly, we manually traced the
781 basal side of epithelial cells from images, and determined discrete sampling points (x_i, y_i)
782 along traced curves at regular intervals. Upon fitting the 4 sampling points from *i*-1 to *i*+2 with
783 a cubic spline function, the function S_i at an interval $[x_i, x_{i+1}]$ was denoted as $S_i(x) =$
784 $a_i(x - x_i)^3 + b_i(x - x_i)^2 + c_i(x - x_i) + d_i$. Due to the definition of the curvature using the
785 formula $\kappa(x) = S''(1 + S'^2)^{-3/2}$, the curvature from the spline function was calculated as
786 follows:
787
788 $$\kappa_i(x) = \frac{6a(x - x_i) + 2b}{(1 + \{3a(x - x_i)^2 + 2b(x - x_i) + c\}^2)^{3/2}}.$$
789
790 The convex/concave surface of the lumen was assigned a positive/negative value, namely κ.
791 We defined tissue thickness as the length from the apical to the basal edge, which is vertical to
792 the traced curve at the sampling points.
793
794 **Mechanical strain assay**
795 We used a mechanical device (STREX, #STB-10) with a polydimethylsiloxane (PDMS)
796 chamber (STREX, #STB-CH-04). To compress isolated epithelium, we placed isolated lung
797 epithelial tissues in a 50% stretched state in the PDMS chamber, and added 1 mL of growth
798 factor-reduced Matrigel (Corning, #356231), and performed gelation for 15 min at 37°C. Then,
799 we added 2 mL of the culture medium supplemented with 500 ng/mL FGF1 into the chamber.
800 We conducted experiments involving epithelial tissues under 2D culture conditions in the
801 following manner. To obtain cell suspensions from primary tissues, lung tissues obtained via
802 dissection at E12.5 were treated with 1 mg/mL Collagenase/Dispase (Sigma-Aldrich,
803 #10269638001) in PBS for 50 min at 37°C while agitating the solution. Lung cells were then
804 dispersed into the solution by gentle pipetting, and the suspended solution was filtered using a
805 40 μm pore size mesh (Corning, #352340). After centrifugation at 200G for 5 min at 25°C, the
806 cell pellet was resuspended in a culture medium containing 10 μM Y-27632 and 10%
807 KnockOut Serum Replacement SR (Thermo Fischer Scientific, # 10828010) and the solution
808 was placed in a PDMS chamber pretreated with a collagen coating (Cellmatrix Type I-C, Nitta

809 Gelatin, #631-00771). After 2 days, the culture medium was exchanged with a medium not
810 containing Y-27632 and KSR, 1 hour before imaging. Notably, the PDMS chamber gradually
811 droops by becoming attached to the silicone oil used for objective lenses, because of which the
812 focus has to be adjusted manually every time an image needs to be obtained.
813
814 **Statistical hypothesis testing**
815 The number of cells or regions of interest analyzed (n) and the number of biological replicates
816 (N) are indicated in the figure legends. No particular statistical method was used to
817 predetermine the sample size. A minimum of N=3 independent experiments were performed,
818 based on previous studies in the field. No inclusion/exclusion criteria were used and all
819 analyzed samples were included in the analysis. No randomization was performed. Statistical
820 tests, sample sizes, test statistics, and *P*-values have been described in the main text. We
821 considered P-values < 0.05 to be statistically significant in two-tailed tests, and classified them
822 into the following 4 categories: * ($p<0.05$), ** ($p<0.01$), *** ($p<0.001$), and n.s. (not significant,
823 i.e., $p \geq 0.05$).
824
825 **Software**
826 We used MATLAB (MathWorks) and Image J (National Institute of Health) software for
827 digital image processing. For graphics, MATLAB (MathWorks), Imaris (Bitplane), and Image
828 J (National Institute of Health) were used. MATLAB (MathWorks) was used for statistical
829 analysis.
830
831 **Graph**
832 In the boxplot, the central mark indicates the median, and the bottom and top edges of the box
833 indicate the 25th and 75th percentiles, respectively. The whiskers extend to the most extreme
834 data points not considered to be outliers, and the outliers are plotted individually using the '+'
835 symbol. All the graphs were drawn using MATLAB.
836
837
838 **(II) Model analysis**
839 **(IIa) Apical length vs cell height at equilibrium**
840 Here, we consider cells in a flat epithelial sheet to be identical, and assume that the basal edge
841 length is almost the same as the apical edge length for the simplicity of analysis. Then, potential
842 energy can be defined as follows:

$$U_{cell} = \frac{k_A}{2}(A - A^*)^2 + \frac{k_a}{2}(a - a^*)^2 + k_l l. \quad (1)$$

The first term represents the cell size constraint and its coefficient k_A, current cell area A, and the target cell area A^*. The second and third terms each represent the regulation of cell edge length at the apical and lateral side of cells a and l with controlling parameters k_a and k_l. We set the second term as a function that converges to the variable target apical length a^*, as explained later. Since the cell size was maintained even after a change in cell shape, caused by the inhibitor assay, we set $A = A^*$. Then, upon considering that $A = rh$, we can redefine equation 1 as follows:

$$U^*_{cell} = \frac{k_a}{2}(a - a^*)^2 + k_l \frac{A^*}{a}, \quad (2)$$

Now, we have two variables, a and a^*, and obtained equilibrium values at the minimum potential energy value, i.e., $a_{eq} = (a|\partial U^*_{cell}/\partial a = 0)$ and $a^*_{eq} = (a^*|\partial U^*_{cell}/\partial a^* = 0)$ each, as $a_{eq} = \sqrt{A^* k_l / k_b}$ and $a^*_{eq} = a_{eq}$. From these equations, it was noted that $a^*_{eq} \sim l^{-1}_{eq}$, which indicates the existence of an inverse relationship between the apical length and cell height at equilibrium. The analysis in this section is based on that of a previous study [64].

(IIb) Apical length vs epithelial sheet curvature

The analysis in this section is based on that of a previous study [65]. Here, we considered the geometrical aspects of an epithelial monolayer, composed of smoothly-connected identical tetragons along a line. The curvature κ at the midplane of the epithelial sheet is represented as

$$\kappa = \frac{2}{a + b}\left(\pi - 2\cos^{-1}\frac{b - a}{2l}\right), \quad (3)$$

where a, b, and l denote the apical, basal, and lateral edge lengths, respectively. Then, the curvature with respect to the apical edge length is determined as follows:

$$\frac{\partial \kappa}{\partial a} = -\frac{2}{l(a + b)\sqrt{1 - \{(a - b)/4l\}^2}} - \frac{2}{(a + b)^2}\left(\pi - 2\cos^{-1}\frac{b - a}{2l}\right) < 0. \quad (4)$$

This indicates that the sheet curvature becomes small with an increase in the apical edge length.

(IIc) Mathematical modeling for multicellular dynamics

We modeled an epithelial monolayer using the vertex model framework [30–32]. In our model, a single cell is represented as a polygon with four vertices and edges, which are shared by neighboring cells. The dynamics of vertex position $\mathbf{r}_i$, where i is an index of the vertex, obeys the equation of motion, based on the principle of least potential energy U, with a drag coefficient η and luminal pressure p as follows:

$$\eta \dot{\mathbf{r}}_i = -\nabla_i U + f(p). \tag{5}$$

To determine the potential energy in the first term, we defined a minimal expression:

$$U = \sum_j \left\{ \frac{k_A}{2}\left(A_j - A_j^*\right)^2 + \frac{k_a}{2}\left(a_j - a_j^*\right)^2 + k_l l_j \right\} + \sum_i \frac{k_\theta}{2}\left\{(\theta_{i_+} - \pi/2)^2 + (\theta_{i_-} - \pi/2)^2\right\}. \tag{6}$$

The first term represents the cell size constraint with its coefficient k_A, current cell area A_j, and the target cell area A_j^*. The second and third terms each represent the regulation of the cell edge length at the apical and the lateral sides of cells a_j and l_j, with controlling parameters k_a and k_l. As the apical edge is controlled by the ERK activation level, we set the second term as a function that converges to the variable target apical length a_j^*; this has been explained later. The fourth and fifth terms represent the bending energy of cells at the apical and the basal sides, attributed to each vertex i; k_θ denotes the bending rigidity, and θ_{i_+} and θ_{i_-} are angles at the vertex i across the cell edge.

The second term of Equation 5 represents the mechanical effect of luminal pressure [34,35,51] on the apical edge of epithelial cells. The function f was defined as

$$f(p) = p\mathbf{n}_i, \tag{7}$$

where p is strength of pressure, and $\mathbf{n}_i$ is the normal vector at the apical vertex i. Note that this function is effective only at vertices in the apical sides of cells.

To implement cell proliferation, we ensured that each cell was set with the cell timer τ_j, and all cells had the same cell cycle length τ_{div}. We assumed that cell cycle progression depended on the curvature; i.e., the cell cycle progresses when the cell curvature is not less than zero ($\kappa_j \geq 0$), and the cell cycle pauses when the cell curvature is less than zero ($\kappa_j < 0$), according to the previous report [36]. This is also attributable to the fact that cell proliferation in the developing murine lung requires ERK activation, which can be observed in the distal tip [23,66]. Cell division occurs and cells with almost equal sizes are produced when the cell timer reaches the cell cycle length, $\tau_j = \tau_{div}$. Once cell division occurs, the τ_j value in one of the daughter cells resets to zero and that in another is set at a value chosen stochastically from 0 to $0.05\tau_{div}$ with a uniform distribution, to avoid perfect synchronization between neighboring cells.

In our model, the target apical edge length depends on the cytoskeletal level c, observed with a level of F-actin accumulation, as follows:

$$a_j^* = \zeta g(c_j) + a_0 \tag{8}$$

$$g(c_j) = \begin{cases} -1, & c_j \leq -1 \\ c_j, & -1 < c_j < 1 \\ 1, & 1 \leq c_j \end{cases} \tag{9}$$

Here, ζ denotes the maximum length after edge extension, and a_0 is the baseline for the apical edge length. The saturation function g represents the physical limit for the change in edge length. We modeled the cytoskeletal level c as follows:

$$\dot{c_j} = \alpha \tanh(\lambda \kappa_j)\, H(\kappa_j) + \beta - \gamma c_j. \tag{10}$$

The first term $\dot{c_j}$ represents the curvature-dependent contribution of FGF-ERK, along with the magnitude parameter α and the sensitivity parameter λ, to the curvature κ. H is the step function of the curvature, i.e., H=1 for $\kappa \geq 0$ and H=0 for $\kappa < 0$. The curvature κ_j at cell j is calculated using the spline function-based method described above. As the cytoskeleton level controls the apical target length observed with an increase in the monotonic function, as shown in Equation 9, curvature-dependent apical extension/shrinkage is represented as a positive/negative α value. The second term represents the curvature-independent contribution

of FGF-ERK, along with the parameter β. The third term represents the decay of cytoskeletons, including F-actin depolymerization and severing. The rate γ controls the characteristic decay time; the inverse value of γ denotes the retention time for cell curvature memory. The level of curvature-dependent FGF-ERK activation was determined in Equation 10 because of its rapid response.

(IId) Numerical simulations

We considered a manually traced line along the basal sides of cells in the image shown in Figure 1 as the initial shape for the simulation, when the diameter of the distal tip *D* was in the measured range. Upon an analysis of the tissue morphology, the number of cells was determined according to the measured cell size, i.e., the average cell width and cell height, which were 5 μm and 20 μm, respectively. The boundary in the proximal side was fixed in the simulations shown in Figures 6B and 6C. For the simulations in Figure 6D–I, we used the symmetrical image created based on the Figure 6A. Ordinary differential equations were numerically solved using the forward Euler method, with a time step of 0.01, using MATLAB (MathWorks). The simulations were terminated when the number of cells was more than 300.

Standard parameters were set as follows: $\eta = 1$, $k_A = 0.01$, $k_a = 1$, $k_l = 0.2$, $k_\theta = 20$, $\tau_{div} = 300$, $\alpha = 1$, $\beta = 0$, $\gamma = 0.001$, $\zeta = 3\ \mu m$, $\lambda = 100$, $p = 0.05$, and $D = 70\ \mu m$, unless otherwise noted. The k_A, k_a, k_l, k_θ, λ, and p values were determined by numerical analyses using several criteria, under which the simulated curvature imitates the experimental observations and became insensitive to the change in the values, as shown in the supplementary figure S4. The maximum length of edge extension, i.e., the ζ value, was determined from our measurements. A_j^* and a_0 values were set according to the initial conditions, e.g., $A_j^* = 93\ \mu m$ and $a_0 = 4\ \mu m$ when $D = 70\ \mu m$.

961 **Supplementary figure legends**

962

963 **Figure S1 3D mapping of ERK activity and tissue geometry**

964 (A) Mapping procedure for linking different quantities, including the ERK activity, epithelial
965 sheet curvature, and sheet thickness. Details of the procedure are described in the Materials
966 and Methods section. (B) The relationship between the ERK activity and discrete mean
967 curvature. $\rho=0.61\pm0.04$, where ρ is Spearman's rank correlation coefficient. Data represent
968 mean and SD values. n=427, N=3.

969

970 **Figure S2 FGF1 endocytosis from the basal side of an isolated lung epithelium**

971 (A) Time-lapse images of the bright field (upper), FGF1-pHrodo (middle), and FGF1-
972 Alexa488 (lower). Red and blue circles in the bright field images indicate the tip apex and the
973 cleft bottom, respectively. The time origin indicates the time of administration of labeled FGF1.
974 FGF1 is distributed only in the Matrigel, not in the lumen, indicating that FGF1 internalization-
975 based endocytosis occurs from the basal side of the epithelium. Notably, FGF1 distribution is
976 almost homogeneous in the Matrigel (lower), indicating that no clear gradient was formed near
977 the epithelium, even after ligand internalization. Scale bar, 50 μm.

978 (B) FGF1-pHrodo intensity at the tip apex (red) and the cleft bottom (blue) over time. The
979 response time of FGF1-pHrodo at the tip apex is 86 min. N=3.

980 (C) FGF1-Alexa488 intensity in the Matrigel over time. The response time of FGF1-Alexa488
981 in the Matrigel is 26 min. N=3.

982

983 **Figure S3 Morphological changes owing to chemical perturbations and cytoskeletal**
984 **architecture**

985 (A) Morphological change in isolated epithelial cells after treatment with 1 μM PD0325901.
986 Colors indicate the ERK activity level. Scale bar, 30 μm.

987 (B, C) Isolated lung epithelium stained with SiR-Actin (B) and with SiR-Tubulin (C). Scale
988 bar, 30 μm.

989 (D) Relative change in cell height after treatment with cytoskeletal inhibitors, such as 1 μM
990 Latrunculin A, 1 μM Nocodazole, and 30 μM Blebbistatin. N≥3 for each treatment.

991 (E–E") Immunofluorescence images of cells interacting with anti-E-cadherin (blue), anti-
992 phospho myosin light chain (pMLC, magenta) and the Hoechst (white) nuclear counterstain.
993 Notably, the pMLC signal is significantly weaker at the tip of the epithelium than in smooth
994 muscle cells around the stalk. In the magnified view (E"), the pMLC signal is clear at the

995 microtubule organizing centers (arrowhead), and is localized at the apical side of cells despite
996 its weak intensity. Scale bars, 100 μm (E, E') and 20 μm (E").
997
998 **Figure S4 Simulation of the mathematical model**
999 (A) Parameter dependency of the monolayer curvature in the simulation.
1000 (B) Relative cell height, normalized by one at α=0, as a function of α. Representative
1001 morphologies of the virtual monolayer sheet are shown in the upper image.
1002 (C) Tissue curvature as a function of luminal pressure p. Representative morphologies of
1003 virtual monolayer tissues are shown in the upper image. N=5.
1004

1005 **Movie legends**

1006

1007 **Movie 1 Volumetric imaging of ERK activity in the murine lung**

1008 The 3D ERK activity map of a murine lung dissected at E12.5. Colors represent the ERK
1009 activity and the color scale corresponds to that in Figure 1B. Scale bar, 50 μm.

1010

1011 **Movie 2 Endocytosis of FGF1 in the isolated lung epithelium**

1012 Time-lapse video of bright field (left), FGF1-Alexa488 (middle), and FGF1-pHrodo (right) in
1013 the isolated lung epithelium embedded within the Matrigel. The color scales correspond to
1014 those in Figure S2A. The time origin indicates the time of administration. Scale bars, 50 μm.

1015

1016 **Movie 3 Dynamics of ERK activity in the growing isolated lung epithelium**

1017 Time-lapse video of bright field (left) and ERK activity (right) during the terminal bifurcation
1018 of an isolated lung epithelium. The color scale corresponds to that in Figure 2D. Scale bars, 30
1019 μm.

1020

1021 **Movie 4 ERK activity response in the isolated lung epithelium to compression parallel to**
1022 **the distal-proximal axis**

1023 Time-lapse video of ERK activity at the tip of the isolated lung epithelium against compression
1024 parallel to the distal-proximal axis. The color scale corresponds to that in Figure 3B. The time
1025 origin indicates the timing of compression. Scale bar, 30 μm.

1026

1027 **Movie 5 ERK activity response of the isolated lung epithelium to compression vertical to**
1028 **the distal-proximal axis**

1029 Time-lapse video of ERK activity at the tip of an isolated lung epithelium against the
1030 compression vertical to the distal-proximal axis. The color scale corresponds to that in Figure
1031 3C. The time origin indicates the timing of compression. Scale bar, 30 μm.

1032

1033 **Movie 6 Morphological change in the isolated lung epithelium by ERK inactivation**

1034 Time-lapse video of ERK activity at the tip of the isolated lung epithelium after treatment with
1035 1 μM PD0325901. The color scale corresponds to that in Figure S4A. Time origin indicates
1036 the timing of inhibitor administration. Scale bar, 30 μm.

1037

1038 **Movie 7 Response of ERK activity and F-actin accumulation to acute simulation with**
1039 **FGF1**
1040 Time-lapse video of ERK activity (left) and SiR-Actin signal (right) at the tip of the isolated
1041 lung epithelium after treatment with 500 ng mL^{-1} FGF1. The color scales correspond to those
1042 in Figure 5A. The time origin indicates the timing of FGF1 administration. Scale bars, 30 μm.
1043
1044 **Movie 8 Simulation for the morphogenesis of the proliferating epithelial monolayer in the**
1045 **regime of curvature-dependent apical extension**
1046 Colors represent the sheet curvature. The color scale corresponds to that in Figure 6E. Scale
1047 interval of the graph is 20 μm.
1048
1049 **Movie 9 Simulation of virtual epithelial monolayer with a short retention time for**
1050 **curvature memory, γ=1**
1051 Colors represent the cellular F-actin levels. The color scale corresponds to that in Figure 6H.
1052 Scale interval of the graph is 20 μm.
1053
1054 **Movie 10 Simulation of virtual epithelial monolayer with a medium retention time for**
1055 **curvature memory, γ= 10^{-3}**
1056 Colors represent cellular F-actin levels. The color scale corresponds to that in Figure 6H. Scale
1057 interval of the graph is 20 μm.
1058
1059 **Movie 11 Simulation of virtual epithelial monolayer with a long retention time for**
1060 **curvature memory, γ= 10^{-6}**
1061 Colors represent cellular F-actin levels in. The color scale corresponds to that in Figure 6H.
1062 Scale interval of the graph is 20 μm.

Figure 1

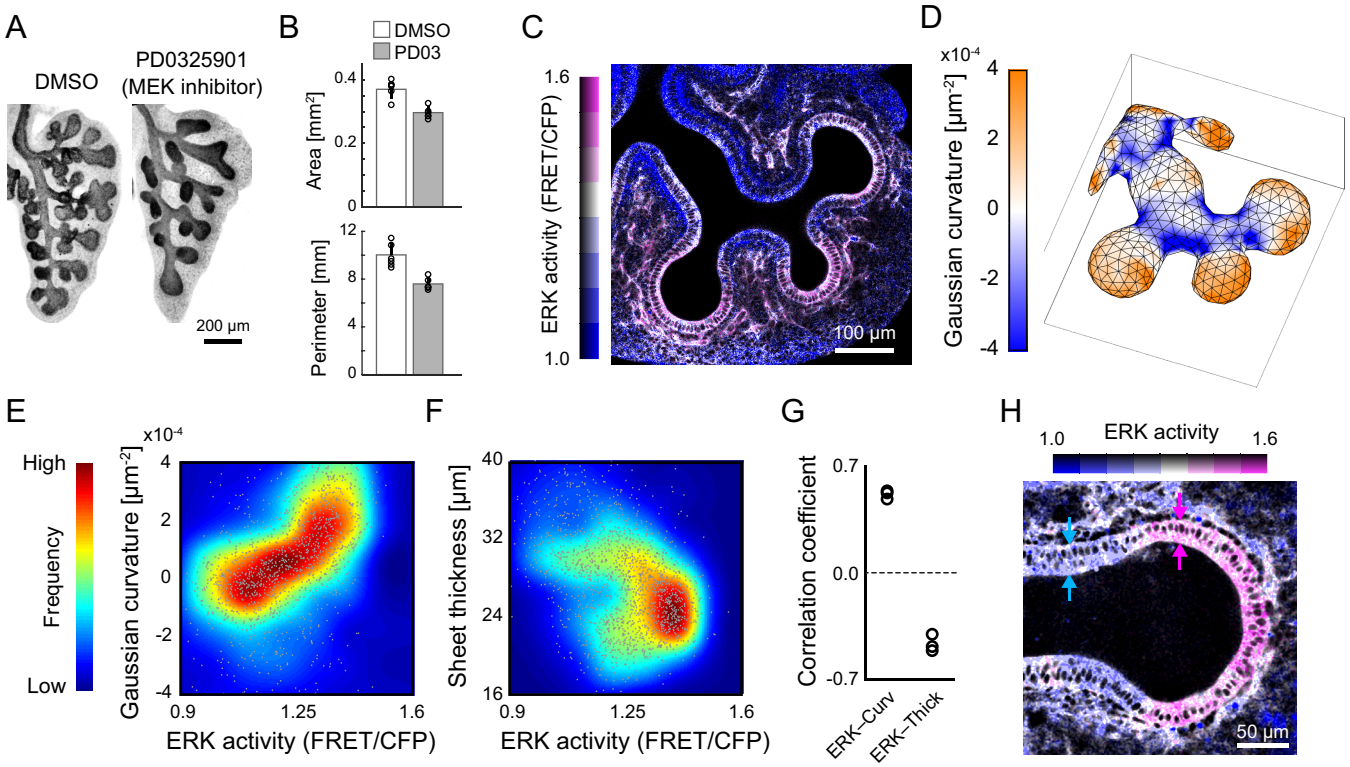
A
DMSO
PD0325901
(MEK inhibitor)
200 µm
B
DMSO
PD03
Area [mm²]
0.4
0.2
0
Perimeter [mm]
12
8
4
0
C
ERK activity (FRET/CFP)
1.6
1.0
100 µm
D
x10⁻⁴
Gaussian curvature [µm⁻²]
4
2
0
-2
-4
E
High
Frequency
Low
Gaussian curvature [µm⁻²]
x10⁻⁴
4
2
0
-2
-4
0.9
1.25
1.6
ERK activity (FRET/CFP)
F
Sheet thickness [µm]
40
32
24
16
0.9
1.25
1.6
ERK activity (FRET/CFP)
G
Correlation coefficient
0.7
0.0
-0.7
ERK–Curv
ERK–Thick
H
1.0
ERK activity
1.6
50 µm

Figure 2

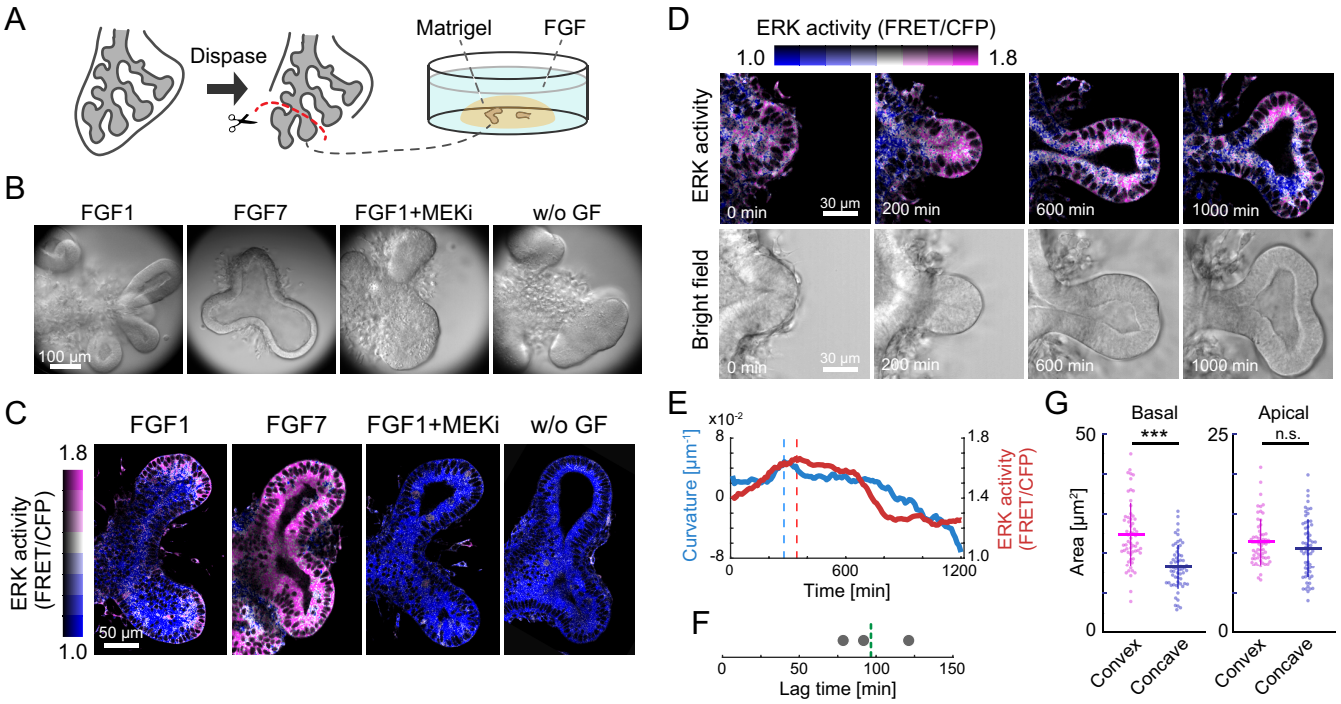
A
Dispase
Matrigel
FGF
B
FGF1
FGF7
FGF1+MEKi
w/o GF
100 µm
C
FGF1
FGF7
FGF1+MEKi
w/o GF
ERK activity (FRET/CFP)
1.8
1.0
50 µm
D
ERK activity (FRET/CFP)
1.0
1.8
ERK activity
Bright field
0 min
30 µm
200 min
600 min
1000 min
E
x10-2
Curvature [µm-1]
ERK activity (FRET/CFP)
Time [min]
F
Lag time [min]
G
Basal
Apical
***
n.s.
Area [µm2]
Convex
Concave

Figure 3

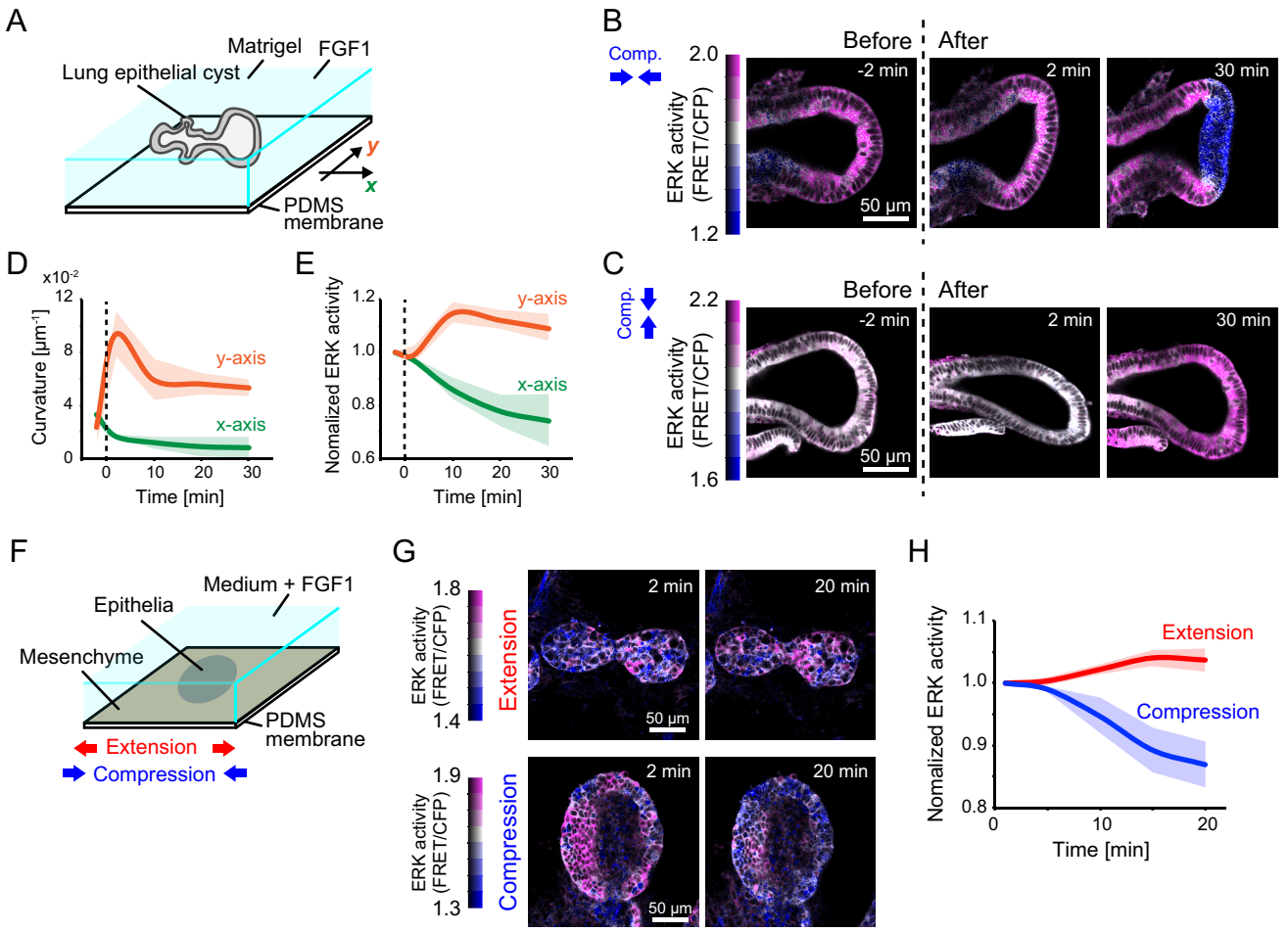
A
Matrigel
FGF1
Lung epithelial cyst
y
x
PDMS membrane
B
Comp.
Before
After
2.0
1.2
ERK activity (FRET/CFP)
-2 min
2 min
30 min
50 µm
C
Comp.
Before
After
2.2
1.6
ERK activity (FRET/CFP)
-2 min
2 min
30 min
50 µm
D
x10-2
12
8
4
0
Curvature [µm-1]
y-axis
x-axis
0
10
20
30
Time [min]
E
1.2
1.0
0.8
0.6
Nomalized ERK activity
y-axis
x-axis
0
10
20
30
Time [min]
F
Medium + FGF1
Epithelia
Mesenchyme
PDMS membrane
Extension
Compression
G
1.8
1.4
ERK activity (FRET/CFP)
Extension
2 min
20 min
50 µm
1.9
1.3
ERK activity (FRET/CFP)
Compression
2 min
20 min
50 µm
H
1.1
1.0
0.9
0.8
Nomalized ERK activity
Extension
Compression
0
10
20
Time [min]

Figure 4

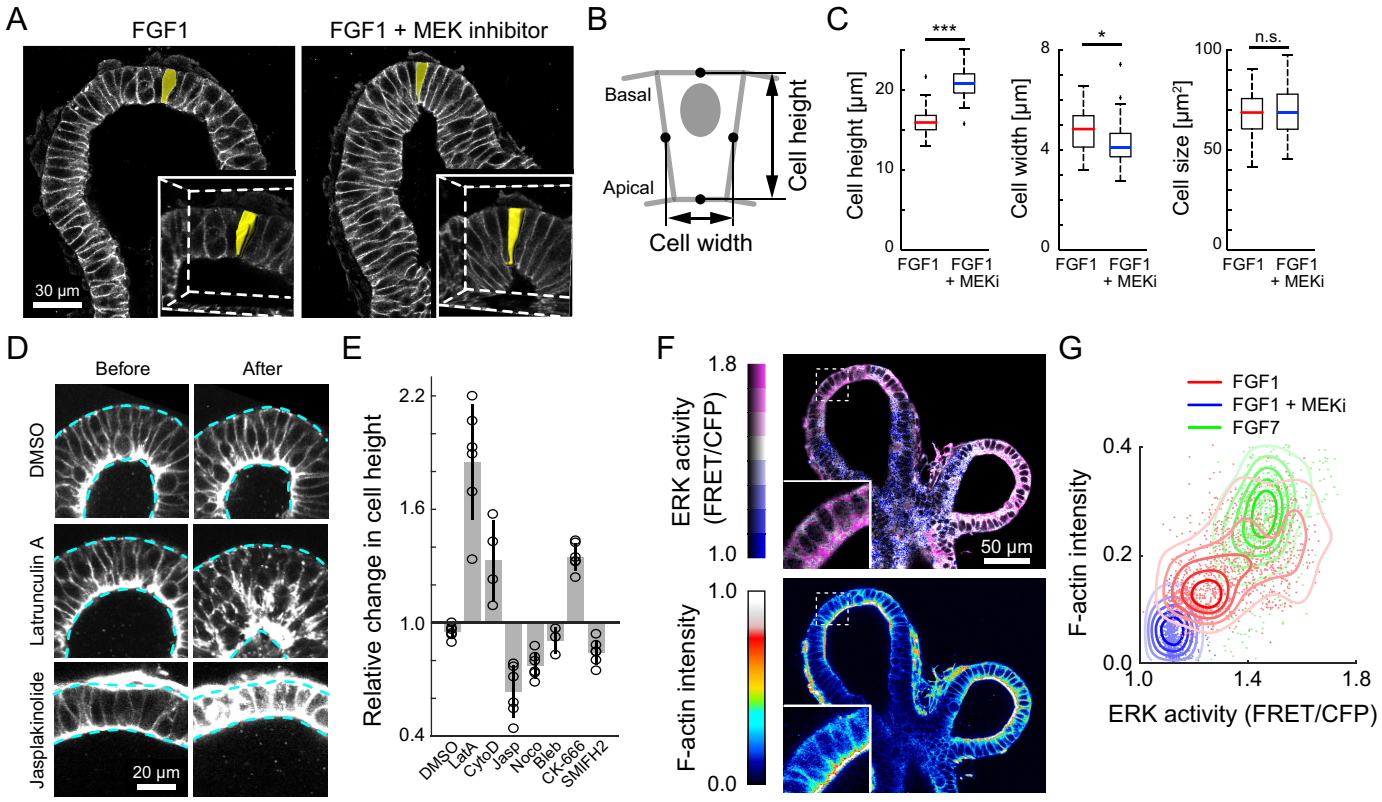
A
FGF1
FGF1 + MEK inhibitor
30 µm
B
Basal
Apical
Cell height
Cell width
C
Cell height [µm]
Cell width [µm]
Cell size [µm²]
***
*
n.s.
FGF1
FGF1 + MEKi
D
Before
After
DMSO
Latrunculin A
Jasplakinolide
20 µm
E
Relative change in cell height
DMSO
LatA
CytoD
Jasp
Noco
Bleb
CK-666
SMIFH2
F
ERK activity (FRET/CFP)
F-actin intensity
50 µm
G
FGF1
FGF1 + MEKi
FGF7
F-actin intensity
ERK activity (FRET/CFP)

Figure 5

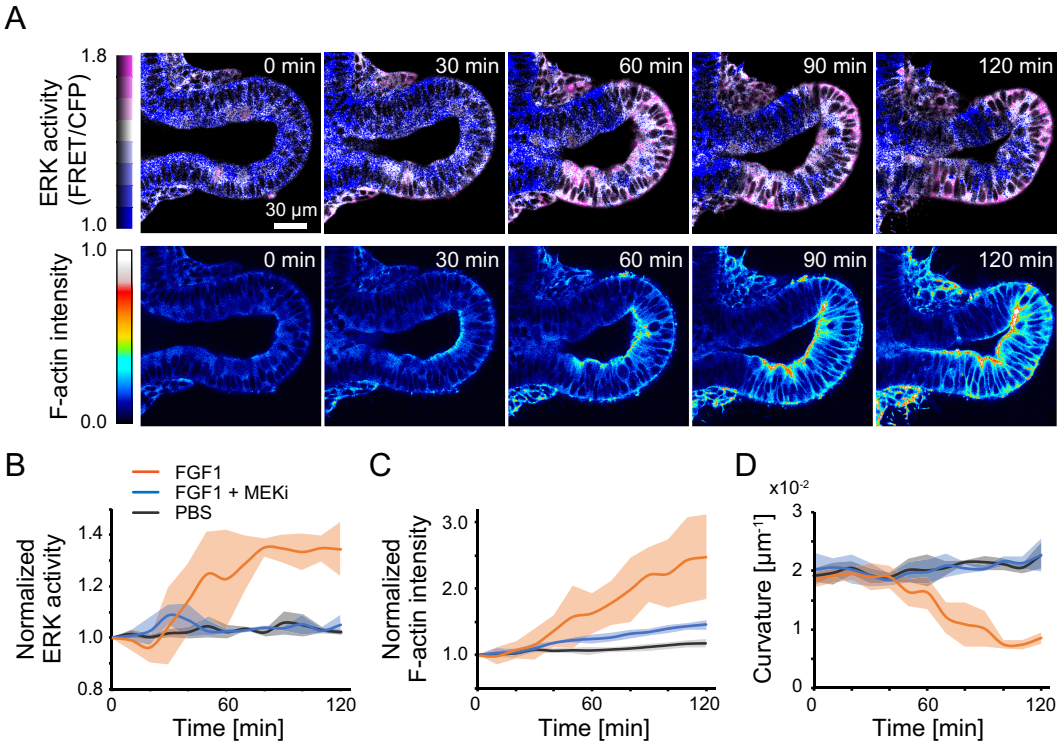
A
ERK activity (FRET/CFP)
1.8
1.0
0 min
30 min
60 min
90 min
120 min
30 µm
F-actin intensity
1.0
0.0
B
FGF1
FGF1 + MEKi
PBS
Normalized ERK activity
1.4
1.2
1.0
0.8
0
60
120
Time [min]
C
Normalized F-actin intensity
3.0
2.0
1.0
Time [min]
D
x10-2
Curvature [µm-1]
3
2
1
0
Time [min]

Figure 6

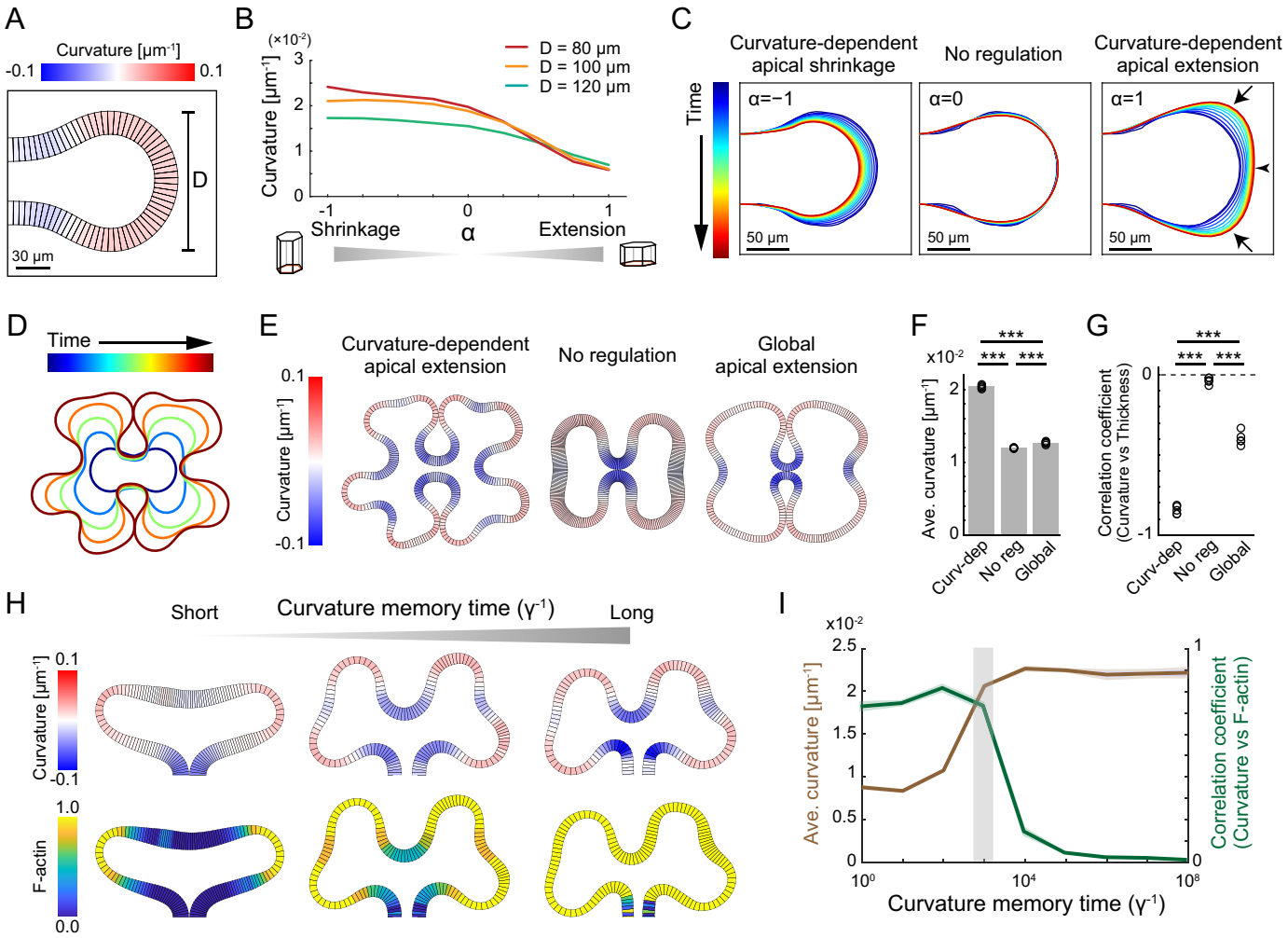
A
Curvature [μm-1]
-0.1
0.1
D
30 μm
B
(×10-2)
Curvature [μm-1]
D = 80 μm
D = 100 μm
D = 120 μm
Shrinkage
α
Extension
C
Curvature-dependent apical shrinkage
No regulation
Curvature-dependent apical extension
Time
α=−1
α=0
α=1
50 μm
D
Time
E
Curvature-dependent apical extension
No regulation
Global apical extension
Curvature [μm-1]
F
x10-2
Ave. curvature [μm-1]
Curv-dep
No reg
Global
G
Correlation coefficient (Curvature vs Thickness)
Curv-dep
No reg
Global
H
Short
Curvature memory time (γ-1)
Long
Curvature [μm-1]
F-actin
I
x10-2
Ave. curvature [μm-1]
Correlation coefficient (Curvature vs F-actin)
Curvature memory time (γ-1)

Figure 7

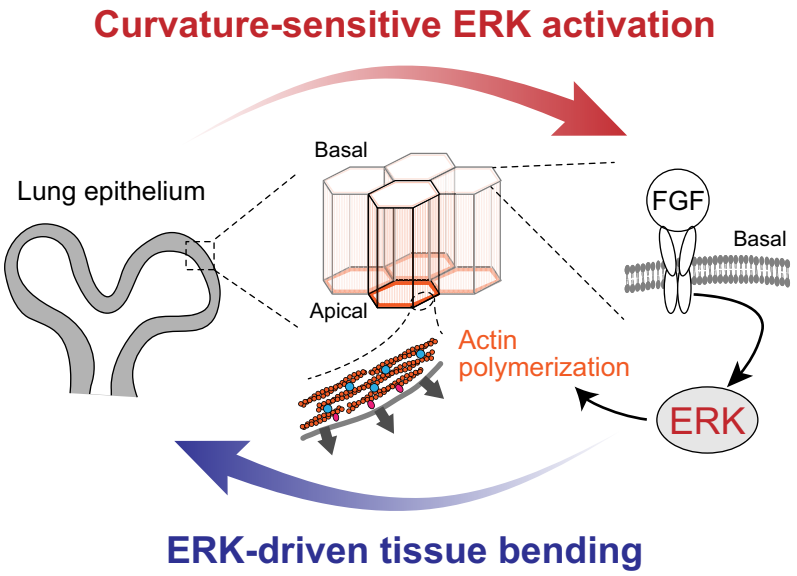
Curvature-sensitive ERK activation
Lung epithelium
Basal
Apical
FGF
Basal
Actin
polymerization
ERK
ERK-driven tissue bending